

# Theoretical Studies of Structure-Function Relationships in $K_V$ Channels: Electrostatics of the Voltage Sensor

Alexander Peyser

November 1, 2021

## Abstract

Voltage-gated ion channels mediate electrical excitability of cellular membranes. Reduced models of the voltage sensor (VS) of  $K_V$  channels produce insight into the electrostatic physics underlying the response of the highly positively charged S4 transmembrane domain to changes in membrane potential and other electrostatic parameters. By calculating the partition function computed from the electrostatic energy over translational and/or rotational degrees of freedom, I compute expectations of charge displacement, energetics, probability distributions of translation & rotation and Maxwell stress for arrangements of S4 positively charged residues and S2 & S3 negatively charged counter-charges; these computations can then be compared with experimental results to elucidate the role of various putative atomic level features of the VS.

A ‘paddle’ model (Jiang et al., 2003) is rejected on electrostatic grounds, owing to unfavorable energetics, insufficient charge displacement and excessive Maxwell stress. On the other hand, a ‘sliding helix’ model (Catterall, 1986) with three local counter-charges, a protein dielectric coefficient of 4 and a  $2/3$  interval of counter-charge positioning relative to the S4  $\alpha$ -helix period of positive residues is electrostatically reasonable, comparing well with *Shaker* (Seoh et al., 1996). Lack of counter-charges destabilizes the S4 in the membrane; counter-charge interval helps determine the number and shape of energy barriers and troughs over the range of motion of the S4; and the local dielectric coefficient of the protein (S2, S3 & S4) constrains the height of energy maxima relative to the energy troughs.

These ‘sliding helix’ models compare favorably with experimental results for single & double mutant charge experiments on *Shaker* by Seoh et al. (1996). Single S4 positive charge mutants are predicted quite well by this model; single S2 or S3 negative counter-charge mutants are predicted less well; and double mutants for both an S4 charge and an S2 or S3 counter-charge are characterized least well by these electrostatic models (which do not include gating load, unlike their biological analogs). Further computational and experimental investigation of S2 & S3 counter-charge structure for voltage-gated ion channels is warranted.

# Contents

<b>1</b>	<b>Introduction</b>	<b>5</b>
<b>2</b>	<b>Methods</b>	<b>9</b>
2.1	Concepts . . . . .	9
2.2	Computing the electrostatics . . . . .	11
2.2.1	Electrical geometry made discrete . . . . .	12
2.2.2	Matrix inversion . . . . .	13
2.2.3	Gauss box: A control for numerical accuracy . . . . .	14
2.2.4	Computation of gating charge . . . . .	14
2.2.5	Electrostatic potential energy . . . . .	15
2.2.6	Maxwell stress . . . . .	17
2.2.7	Statistical mechanics . . . . .	17
2.3	Details of the simulation environment . . . . .	17
2.3.1	Sliding helix model . . . . .	18
2.3.2	Paddle model . . . . .	18
<b>3</b>	<b>Results and Discussion</b>	<b>22</b>
3.1	A ‘paddle’ model . . . . .	22
3.2	A ‘sliding helix’ model . . . . .	26
3.3	Which model features are important for voltage-sensing by a sliding helix? . . . . .	30
3.3.1	Counter-charges eliminate the induced-charge barrier . . . . .	30
3.3.2	Counter-charge spacing matters . . . . .	30
3.3.3	Electrical polarizability of the protein controls effective gating charge . . . . .	32
3.4	Charge mutations act via charge/counter-charge interactions . . . . .	34
3.4.1	Mutation of a positive charge . . . . .	39
3.4.2	Mutation of a negative charge . . . . .	39
3.4.3	Combined mutations of a positive and a negative charge . . . . .	39
3.4.4	Investigation of a mutant lacking functional expression . . . . .	39
3.4.5	Summary of mutation simulations . . . . .	39
<b>4</b>	<b>Perspectives</b>	<b>46</b>

# List of Figures

1.1	Computation of action potential . . . . .	6
1.2	Topology . . . . .	6
1.3	Crystal structure . . . . .	8
2.1	Simulation cells . . . . .	12
2.2	Source charges and dielectric boundaries: Sliding helix . . . . .	19
2.3	Source charges and dielectric boundaries: Paddle . . . . .	20
2.4	Configurations of charges in sliding helix models . . . . .	21
3.1	Paddle: Stability in membrane . . . . .	24
3.2	Paddle: Maxwell stress . . . . .	25
3.3	Sliding helix: Potential energy landscapes . . . . .	27
3.4	Sliding helix: Maxwell stress . . . . .	28
3.5	Sliding helix: Action of voltage . . . . .	29
3.6	Counter-charges: Energetically required . . . . .	31
3.7	Counter-charge spacing: Potential energy landscapes (Pt. 1) . . . . .	32
3.7	Counter-charge spacing: Potential energy landscapes (Pt. 2) . . . . .	33
3.8	Counter-charge spacing: Electrostatic barriers & wells . . . . .	34
3.9	Counter-charge spacing: Statistical mechanics . . . . .	35
3.10	Dielectric coefficient: Potential energy landscapes . . . . .	36
3.11	Dielectric coefficient: Size of potential energy barriers . . . . .	37
3.12	Dielectric coefficient: Displacement . . . . .	37
3.13	<i>Shaker</i> : <i>R362Q</i> . . . . .	40
3.14	<i>Shaker</i> : <i>R365Q</i> . . . . .	40
3.15	<i>Shaker</i> : <i>R368N</i> . . . . .	41
3.16	<i>Shaker</i> : <i>R371Q</i> . . . . .	41
3.17	<i>Shaker</i> : <i>E283Q</i> . . . . .	42
3.18	<i>Shaker</i> : <i>D316N</i> . . . . .	42
3.19	<i>Shaker</i> : <i>E293Q</i> . . . . .	43
3.20	<i>Shaker</i> : <i>K374Q</i> + <i>D316N</i> . . . . .	43
3.21	<i>Shaker</i> : <i>K374Q</i> + <i>E293Q</i> . . . . .	44
3.22	<i>Shaker</i> : <i>K374Q</i> (Imaginary) . . . . .	45

# List of Supplementary Material

Movie: tile-helix-side.mp4 . . . . .	19
Movie: tile-helix-top.mp4 . . . . .	19
Movie: tile-paddle-side.mp4 . . . . .	20
Movie: tile-paddle-top.mp4 . . . . .	20
Movie: flat-paddle.mp4 . . . . .	25
Movie: flat-s4.mp4 . . . . .	28

# Chapter 1

## Introduction

Electrical excitability of cells is possible because the movement of a few charges can control the flow of many charges. This principle – amplification – led Hodgkin and Huxley (1952b) to their theory of the action potential in terms of electrically controlled membrane conductances (for an example of a computation of their model, see Fig. 1.1). Such conductances have been localized to channel proteins conducting  $\text{Na}^+$ ,  $\text{K}^+$ , or  $\text{Ca}^{2+}$  ions. Besides a conductive port (composed of transmembrane domains S5 and S6, see Fig. 1.2), the channels contain four transmembrane regions (labeled S1-S4 starting from the amino end). In the S4 region, there are a total of three to seven positively charged amino acid residues, each arrayed at every third amino acid position. An extensive electrophysiological data set exists on voltage-controlled ionic conductance and the ‘gating current’ attributable to charges controlling the ionic port. A second extensive data set has emerged from experiments measuring structure. Both sets provide essential perspectives, but no direct means to assess physical interactions in the structure and the significance of physical interactions for function. In this thesis, I attempt to bridge these perspectives computationally. I focus on electrostatics because the voltage-gated ion channels are controlled by an applied electric field that acts on intrinsic protein charges.

Voltage-gated  $\text{K}^+$  channels ( $\text{K}_v$ ) are composed of two distinct functional elements, a ‘voltage sensor’ and a ‘pore domain’. As described by Lee et al. (2005), they appear to be “membrane proteins with separate, weakly attached membrane-spanning domains”.  $\text{K}_v$  channels may have evolved as the concatenation of two separate proteins, one contributing a central tetrameric  $\text{K}^+$  conducting pore and the other contributing a weakly-attached peripheral voltage sensor which transduces changes in transmembrane

potential into a flow-controlling action on the pore domain (Kumanovics et al., 2002). The voltage sensor motif is homologous with voltage-sensitive proton conducting channels ( $\text{H}_v$ , Ramsey et al., 2006). The physics underlying the well-known function of the  $\text{K}^+$  and related  $\text{Na}^+$  and  $\text{Ca}^{2+}$  channels (Hodgkin and Huxley, 1952a; Catterall, 1988) in terms of the atomic structures developed over the last 20 years (Doyle et al., 1998; Jiang et al., 2003) has still not been fully elucidated. Questions are still open regarding the precise electrostatics, thermodynamics and distributions of relative positions & motions of charges at physiological temperatures.

Each voltage sensor comprises four largely helical secondary structures. The S4  $\alpha$ -helix bears a positively charged arginine or lysine residue at every third position while the S2 and S3 helices bear a smaller number of negatively charged aspartate or glutamate residues (Noda et al., 1986). The other residues of these membrane-spanning segments are mostly hydrophobic. It has been proposed that the transmembrane electric field moves the S4 segment through a combination of translation and rotation with respect to the other helices and the lipid membrane (‘sliding helix’ hypothesis, Catterall 1986), or alternatively moves the S4 segment in association with part of the S3 segment across the lipid much like a large lipophilic ion (‘paddle’ hypothesis, Lee et al. 2003).

In both proposed mechanisms, multiple electric charges of the channel protein move in the electric field of the membrane and therefore produce a displacement current (‘gating current’, Hodgkin and Huxley, 1952b; Chandler and Meves, 1965; Armstrong and Bezanilla, 1973), as well as electric work which could drive gating of ionic conductance (Hodgkin and Huxley, 1952b). Translocation of these charges could be facilitated by factors such as a local thinning of the lipid

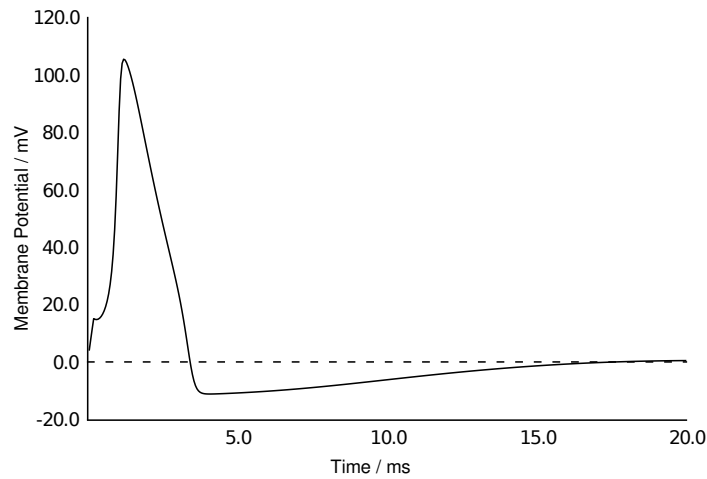


**Figure 1.1: Computation of an action potential** according to the Hodgkin and Huxley (1952b) model (comparable to Fig. 13, upper curve, same paper). This curve is calculated with  $I = C_M \dot{V} + \bar{g}_K n^4 (V - V_K) + \bar{g}_{Na} m^3 h (V - V_{Na}) + \bar{g}_i (V - V_i)$  [Eq. 26, same paper], using the same constants as the original paper for activation, inactivation, reversal potentials and conductances. The variables  $n$ ,  $m$  and  $h$  represent the proportion of 'activating or inactivating particles' for a channel in the activating position:  $n$  for the activating  $K^+$  channel particles;  $m$  for the activating  $Na^+$  channel particles; and  $h$  for the inactivating  $Na^+$  channel particles. Since the rate constants for the first derivative of these variables were voltage dependent, the physical interpretation was of a charge-carrying voltage sensor driving the opening and closing of ionic conductance.

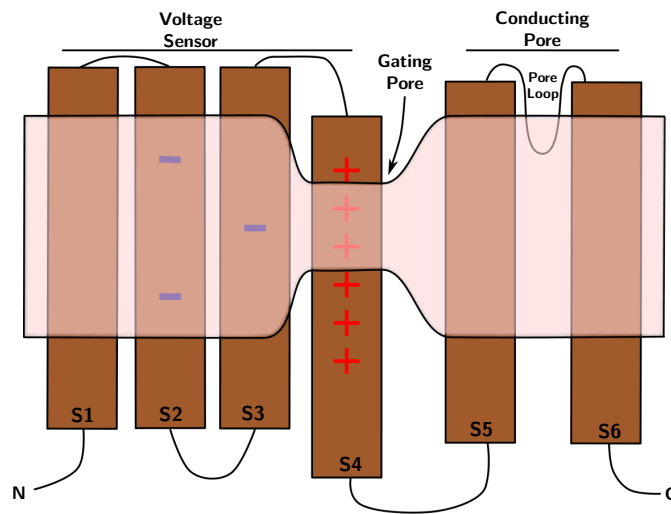


**Figure 1.2:  $K_v$  channel schematic topology:** a generic  $K_v$  channel representation highlights the transmembrane domains of a single unit of the  $K_v$  tetramer. On the left from the amino end of the protein are the voltage-sensor domains, S1–S4. On the right are the conducting pore domains, S5 and S6. The lipid bilayer through which the protein is threaded is represented in pink. The red '+' symbols represent the excess positively charged amino acid residues on S4 that are believed to cross the lipid bilayer at the invagination labeled 'gating pore'. The blue '-' symbols represent excess negatively charged amino acid residues on the S2 and S3 transmembrane domains.

bilayer, a reduction of the passage-way to a short ‘gating pore’ (Parsegian, 1969; Perozo et al., 1993) or the provision of counter-charges along the route of the moving S4 charges by static residues of S2 and S3. The existence of a short gating pore is indicated by the accessibility of modified S4 positions to extra- or intracellular cysteine reactants or protons (Yang et al., 1996). The relevance of counter-charges has been indicated by neutralization mutants (Seoh et al., 1996) and coordination of S4 charges with residues of opposite charge in recent crystallographic studies (Long et al., 2007).

An understanding of the natural design of the voltage sensor needs to be based on a broad exploration of the components that have been discovered experimentally. The importance of design elements that have emerged from these experiments should be evaluated. How do such elements determine sensor characteristics? How do their specific evolutionary layouts bring about voltage sensor behavior as seen in different channel types? And as an important control, can results of experimental mutations be predicted?

It is tempting to base exploration of a molecular device like the voltage sensor solely on available information of atomic structures, as represented in Fig. 1.3. The study of atomic structures, however, is greatly limited in the case of the voltage sensor. Crystallization destroys the natural (dielectric) environment of the structure and in particular the electric field that the structure is designed to detect. Atomic-level computations like those based on Molecular Dynamics (MD) are speculative to the extent that they are based on questionable atomic coordinates. Moreover, they are currently restricted to explorations of sub-microsecond episodes of dy-

namics of a few chosen initial configurations (Khalili-Araghi et al., 2010).

In this thesis, I analyze reduced electrostatic models (see CONCEPTS, SEC. 2.1) for the voltage sensor which can be thoroughly specified: charged rigid bodies moving through piecewise homogeneous dielectric domains. The sensor model is embedded in a simulation cell mimicking a voltage-clamp setup including electrodes, allowing macroscopically observed variables to be predicted from the microscopic model. The electrostatics are solved self-consistently with numerical methods that allow systematic exploration. Specifically, my computations construct an electrostatics-based partition function of charge configuration with two degrees of freedom: rotation and translation of the S4 segment. Using this partition function, I compute the expectation of random variables such as charge displacement in response to voltage for comparison with experiment. These measures have not been accessible in other computational studies (Bliznyuk and Rendell, 2004; Chakrapani et al., 2008; Nishizawa and Nishizawa, 2008; Khalili-Araghi et al., 2010).

My results show that a voltage sensor (VS) model involving a sliding S4 helix is realistic with respect to both gating charge and electrostatic energetics. A crucial component of this model is negative counter-charges arranged in close proximity to buried S4 charges. The electrostatic design of this VS tolerates considerable variation resulting in electrophysiologically interesting variations of sensor characteristics. Simulations of S4, S2 and S3 charge mutants in this electrostatic model predict experimentally observed patterns of charge displacement (Seoh et al., 1996).

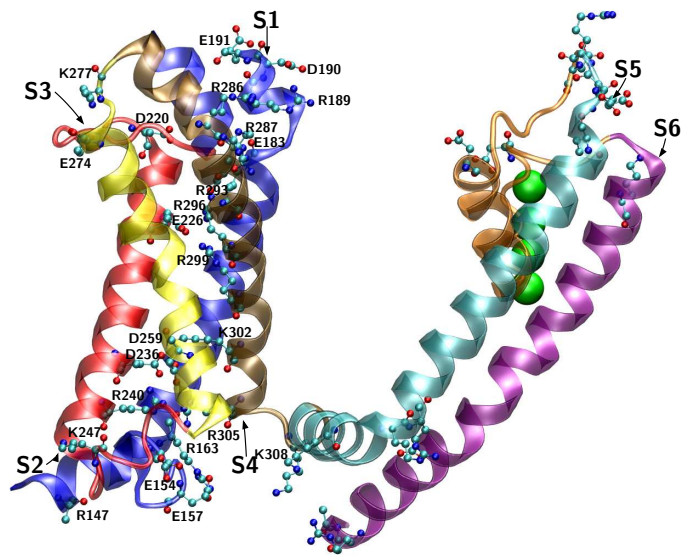


**Figure 1.3: Crystal structure of a chimeric  $K_v$  1.2 and  $K_v$  2.1  $K^+$  channel** (Long et al., 2007, PDB No. 2r94). This single unit of the channel tetramer is composed of  $K_v$  1.2 channel elements with S4 and parts of S3 replaced by homologous regions from  $K_v$  2.1. The backbones of S1–S4 are represented by ribbons; charged residues (arginines, lysines, glutamates and aspartates) are represented in ball-and-stick format. The approximate S1 region ribbon is in blue; S2 is in red; S3 is in yellow; S4 is in brown; S5 is in cyan; S6 is in purple; and the pore loop is in orange.  $K^+$  ions near the pore loop are represented by green spheres. Charged residues which may be part of the voltage sensor (S1–S4) are labeled by their residue number for this chimera. Graphic produced with VMD (Humphrey et al., 1996)



# Chapter 2

## Methods

My approach to voltage sensor electrostatics has three major elements: (1) I use *reduced* physical descriptions of electrostatic components; (2) I compute predictions that correspond to *experimental conditions and observables*; and (3) I develop a *statistical-mechanical description* of sensor behavior by exploring a wide range of sensor configurations.

### 2.1 Concepts

**Reduced descriptions.** By a ‘reduced model’, I mean a model where some details are reduced in resolution; for example, in electrostatic models many charge distributions are reduced to dielectric constants or tensors. The selection of which features are to be reduced and which are to be represented at higher resolution is an iterative problem involving the identification of the relevance of those features to the measures of interest. All models that are not calculated by *ab initio* quantum mechanical calculations are reduced in this sense. By explicitly structuring a model with multiple tiers of resolution and identifying the relevance of those components of the system to measures of interest, it is possible to distinguish the dominant terms in the underlying physics.

Atomic matter is made of charged constituents, charged nuclei and charged electrons (Feynman et al., 1963). The crucial charges for this study are the uncompensated nuclear charges in the arginine or lysine side chains of the S4 region and the excess electronic charges of the glutamate and aspartate side chain in the S2 and S3 regions (Creighton, 1984; Islas and Sigworth, 1999), out of the vast number of nuclei and electrons in the system. Most of the ‘vast number’ of charges form neutral atoms or molecules, but at close range many molecules reveal spatial asymmetries in their internal charge distributions. Moreover, the electric field from other

components can distort the internal charge arrangements of molecules or groups that are overall neutral into asymmetrical distributions of charge. Both the rotational alignment of molecules with internal charge asymmetry and the distortion of symmetrical charge distributions in molecules are abstracted as ‘polarization.’ Polarization of matter in an electric field ‘induces’ charge that is hidden in the absence of the field (Griffiths, 1999c, see Fig. 22). The most abundant polarizable molecule in VS system is the water of the solutions bathing the membrane.

An *ab initio* (quantum mechanical) description of the charged nuclei and electrons in a channel protein, membrane, and embedding ionic solutions is not possible — approximations must be made. Approximate physical descriptions can be made in multiple tiers of resolution: either the results of lower tiers become parameters for higher-tier theory, or independent experimental results produce parameters for higher tiers. For example, an ion is an atom or molecule in which the number of nuclear elementary charges is not identical to the number of electron charges. A classical approximation for an atomic ion is a point charge at the center of a sphere where the effective diameter of the sphere that excludes other atoms can be determined from crystallographic measurements. I use such a classical description for formal charges explicitly included in models.

Polarization of neutral molecules and groups must also be described by approximations. Voltage sensor charges buried in the membrane polarize bath water. A reasonable starting point for a description of that polarization is a continuum description of the water. A space element containing polarizable molecules will exhibit polarization charges on its surfaces when an electric field is present (Boda et al., 2004). These surface charges represent the polarization of

the molecules in the space element: if these charges are included in a computation of the electric field, the molecular polarization is accounted for. The amount of polarization charge is proportional to the strength of the applied field (over a range), and depends on the atomic/molecular composition of the matter in the space element. In the linear range, the polarization charge at the surfaces of the space element is related to the field strength by a material coefficient (or tensor for anisotropic polarization). Water polarization can be described this way by one number, the dielectric coefficient. Furthermore since polarization involves a rearrangement of charges, polarization takes a finite amount of time to develop or disappear. However, since voltage sensor relaxations are slow compared to typical polarization relaxations, polarization can be approximated as instantaneous. For instance, the rotational relaxation time of water is on the order of  $10^{-11}$  s (Barthel et al., 1995), while voltage sensor relaxation times are on the order of  $> 10^{-5}$  s (Hille, 2001; Sigg et al., 2003).

The channel and membrane are bathed in electrolyte solutions on either side. Electrostatic interactions involving bath ions are reduced two orders of magnitude by the solvent (water) with respect to the vacuum. This reduction is described by the dielectric coefficient of water. Furthermore, ions screen one another to an ionic concentration-dependent extent. Screening arrangements in solutions form in nanoseconds (Barthel et al., 1995), which is much faster than the time base for VS motion — like polarization, screening can be approximately described as instantaneous.

Screening by bath ions is modeled in my simulation cells by placing the electrodes closer to the membrane than would be done in an experiment. A diffuse layer of screening counter-ions is electrostatically equivalent to counter-charge smeared on a surface a Debye length from the screened charge, which is the essential result of the Debye-Hückel and Gouy-Chapman descriptions of screening (Debye and Hückel, 1923; Gouy, 1909; Chapman, 1913). By varying the distance between the membrane and the screening electrode surface, variations of bath ionic strength can be mimicked (for example, offsets of 3 nm and 0 nm bracket the Debye lengths of dilute [3 mM] and infinitely concentrated solutions<sup>1</sup>). In the simulations reported here I use the electrode geometries of Fig. 2.1, roughly equivalent to bath solutions containing 3 mM salt. Experimental vari-

ation of bath ionic strength has relatively small effects on experimental gating currents (Islas and Sigworth, 2001). Indeed, control computations (not shown) in which the water domain is removed from the simulation and the electrodes are placed directly on the membrane and protein surfaces (to mimic infinite ionic strength) yield results similar to those obtained with the simulation cells of Fig. 2.1.

**Coupling microscopic VS motion to macroscopic experiments.** Computer experiments provide insights into microscopic systems that are difficult if not impossible to obtain by conventional experiments. To estimate the functional competence of hypothetical structures, experimental observables of function must be computed, and conditions comparable to conventional experimental conditions must be established. Gating current, the most direct observable reporting VS motion, is recorded experimentally while applying a prescribed voltage across electrodes placed in the electrolytes bathing the membrane (a voltage clamp). My computational setup is designed to establish a voltage clamp and record the charge displaced by VS motion in a manner comparable to charge displacement recordings with macroscopic electrodes.

**From electrostatics to statistical mechanics.** The primary results of my computations are the electrostatic potential energy and gating charge corresponding to a particular location of the formal charges of the voltage sensor model at a particular applied voltage. (Another output is the Maxwell stress, see below in MAXWELL STRESS, SUBSEC. 2.2.6). The efficiency of my computational methods allows me to compute these variables for a very large number of VS configurations and applied voltages, thus enabling me to elaborate a statistical (thermodynamic) view of VS configuration.

I explore a configuration space that includes the rotation of the S4 helix about its axis and the translation of the S4 charges along that axis at a fixed applied potential. A partition function in those configurational degrees of freedom is constructed from the ensemble of Boltzmann factors for each electrostatic potential energy. Using the partition function, statistical expectations of equilibrium positions and displaced charges are obtained. In this way, I determine both how the model will configure at a particular membrane voltage, and along which average configurations the model will re-configure as voltage is varied in small increments — these are equilibrium averages and not trajec-

<sup>1</sup>See Fig. 3 on pg. 3718 under *Defining electrical coordinates and electrical travel* of Nonner et al. (2004)

tory calculations. The relation between gating charge and voltage is predicted, allowing comparison with experimental charge/voltage curves recorded from ensembles of voltage sensors.

**The typical simulation cell.** A typical geometry for a computational experiment is shown in 2.1 (a). The simulation environment is represented by an axial cross-section of the radially symmetric three-dimensional domain swept by rotating that cross-section about its vertical axis. The hemispheric boundaries (in green) are electrode surfaces kept at controlled electrical potentials. The blue zones represent aqueous baths (with a dielectric coefficient  $\epsilon = 80$ ). The pink zone is a region of small dielectric coefficient ( $\epsilon = 2$ ) that represents the lipid membrane. The brown zone represents both the non-S4 components of the VS protein and the matrix of the S4 helix (the central cylinder). The helix crosses the membrane through a ‘gating pore’ which extends the baths into the region joining S4 and the rest of the protein. The dielectric coefficient of this protein region is varied in my simulations to assess its importance for VS motion. The dielectrics in this reduced model are piecewise uniform and therefore have sharp boundaries (solid black lines). Point charges representing S4 and other charges (not shown) are embedded in the region of protein dielectric.

VS motion is simulated in this geometry by *moving only the S4 charges* within the fixed cylinder bounding the S4 helix. Simulating S4 motion this way (by moving charges and not dielectric boundaries) greatly reduces the computational costs of solving the electrostatics since solving for the effects of moving dielectric boundaries requires recomputing the matrix inversion (see MATRIX INVERSION, SUBSEC. 2.2.2). The dielectric geometry as defined is invariant in terms of rotation. Only the end caps of the S4 are not invariant in terms of central-axis translation. If those ends of the biological S4 are translated, which is not well defined experimentally, then the positionally fixed end-points of the S4 in these simulations would not capture the movement of surface charge on those S4 ends. However, the surface charge on those ends would move outside the region of high electrical travel close to the gating pore (Nonner et al., 2004, Fig. 1), therefore adding little to either the charge displacement terms or the associated energy terms. Charge/end-surface interaction terms could only become significant at the extrema of S4 charge motion along the central axis.

## 2.2 Computing the electrostatics

My general approach for computing the electric field in this system is to superpose the vectorial Coulombic fields of all charges. Likewise, the electrical potential is computed by scalar superposition of the Coulombic potentials of all charges (Jackson, 1999b, section 3). The contributions to the field made by the S4 and other formal charges at known positions are readily computed, but the charges on the electrodes and the polarization charges at dielectric interfaces are initially unknown. The determination of the contribution of surface charges is a crucial (and computationally expensive) element of solving the electrostatics.

Since dielectrics are involved, a precise definition of ‘charge’ is needed for the following mathematical treatment. I follow the nomenclature of Jackson (1999a), who distinguishes between ‘source’ and ‘induced’ charges. The formal charge on a side-chain of the S4 region (one proton charge) is a source charge, as are charges placed by the external voltage clamp circuit on the electrodes. Induced charges comprise those charges appearing on dielectric boundaries in response to the fields of source charges and other induced charges. It is convenient to combine spatially inseparable source and induced charges into ‘effective’ charges. Specifically, I assign to a point source charge ( $q_s$ ) embedded in a dielectric ( $\epsilon$ ) an effective charge ( $q = q_s/\epsilon$ ), combining the source charge and the polarization induced at the dielectric boundary around that source charge ( $-q_s(\epsilon-1)/\epsilon$ ). In other words, the effective point charge is the sum of the source and induced charges, expressing the fact that the field produced by a source charge in a dielectric is  $\epsilon$  times weaker than the field of the source charge in vacuum. Electrode charges are also represented in computations by effective charges, which eliminates the need to specify polarizable matter outside the cell. Finally, induced charge on a dielectric boundary separated from any source charge is formally treated as an effective charge (lacking a source charge component). Thus, *all* charges are expressed in computations as effective charges. The field computed from effective charges is identical to the superposition of the fields of the source charges and their polarization charges. That superposition of fields is the field that must be computed for the computer experiments presented here.

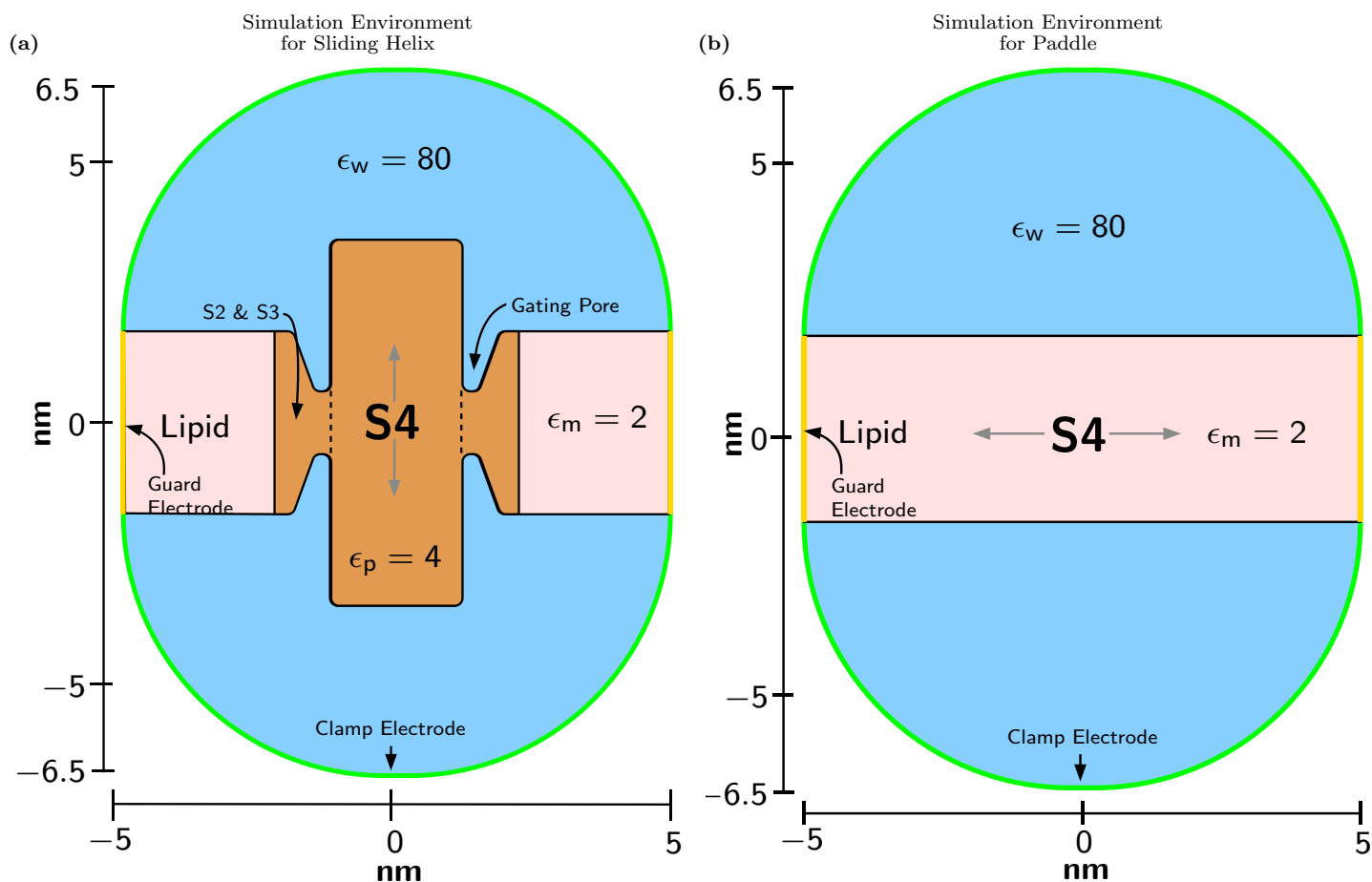


**Figure 2.1:** Cross-sections of the simulation cells for the sliding helix model (a) and the paddle model (b). The 3D setup is produced by rotating the cross-section about its vertical axis. The setup is bounded by two hemispherical bath electrodes (in green). Their potentials are maintained at prescribed values as the S4 segment is moved (voltage clamp). The cylindrical electrode (in gold) completing the boundary is a guard. It is divided into rings maintained at potentials that are linearly graded between the potentials of the bath electrodes. The interior is divided into two aqueous baths (in blue) separated by a lipid membrane (in pink) and, in the sliding helix model, a VS protein region (in brown) forming a gating pore around the sliding S4 helix. In the paddle model, no distinction is made between membrane and protein — the S4 charges (not shown) are embedded in the membrane. The charge configuration of the sliding helix model is shown in Fig. 2.2.

## 2.2.1 Electrical geometry made discrete

To compute the charges on the electrodes and dielectric boundaries, the boundary surfaces are tiled into curved quadrangular surface elements (Fig. 2.2 for the sliding helix model & Fig. 2.3 for the paddle model). The size of these surface elements is chosen such that the charge density present on an element can be approximated as uniform

on the element. Properly choosing the tile size to conform to that approximation requires numerical controls described later (GAUSS BOX, SUBSEC. 2.2.3). There is one unknown to be determined for each surface element: its surface charge. Below, I will show how one linear equation can be obtained per surface element. Solving the system of these linear equations yields all unknown charges, which typically involves 4000–10000 surface elements of different sizes (and that number of

unknowns) for numerical accuracy (checked by Gauss' law to recover the total integral number of charges within volumes surrounded by closed surfaces, see GAUSS BOX, SUBSEC. 2.2.3).

The electrodes impose voltage clamp conditions. In the discrete representation of the electrode surface, the potential at the center of an electrode element ( $i$ ) assumes a prescribed value ( $V_i$ ). The potential at the center of that element results from the superposition of the potentials due to *all* charges ( $j$ ), including that of element  $i$  itself:

$$V_i = \frac{1}{4\pi\epsilon_o} \sum_j \frac{q_j}{|\mathbf{r}_{ij}|} \quad (2.1)$$

The definition of the distance  $|\mathbf{r}_{ij}|$  for a surface charge  $j$  depends on the distance of that element from element  $i$ . The surface charge of a distant element is combined into a single point charge located at the charge center of that element, and  $|\mathbf{r}_{ij}|$  is defined as the distance between those points. The surface charge of a proximate element (in particular, element  $j = i$  itself) is divided into smaller charges obtained by sub-tiling element  $j$  into a number of subelements (typically  $4 \times 4$  for  $j \neq i$ , and  $10 \times 10$  for  $j = i$ ). Each subelement carries a fraction of element  $j$ 's charge, and  $1/|\mathbf{r}_{ij}|$  is defined as equal to the weighted average by subelement area of the inverse distances for all subelements to the center of  $i$ . The subelements follow the curvature of the surface element.

A correct representation of surface curvature and the curvature's effects on charge distribution is crucial for numerical accuracy. Inhomogeneities in charge distribution are particularly problematic when source or other induced charges are close to the surface element. If the element has curvature, the charge induced on one part of the element will induce charge at close range on other parts of the same element. Inaccuracies due to charge inhomogeneity and surface curvature are limited by choosing an adequate initial tiling and sub-tiling as needed.

The boundary condition describing the effect on the field due to dielectric boundary elements can be expressed in two equivalent ways. One way of describing the boundary condition is that the normal components of the field strengths on each side of the boundary ( $\mathbf{E}_1^\perp$  and  $\mathbf{E}_2^\perp$ ) are inversely related to the dielectric coefficients of each region (Griffiths, 1999c, 40):

$$\epsilon_1 \mathbf{E}_1^\perp = \epsilon_2 \mathbf{E}_2^\perp \quad (2.2)$$

The other expression for relating normal field strengths says that the field strengths differ by the field of the polarization

charge induced on the surface (Jackson, 1999c, 22):

$$\mathbf{E}_1^\perp + \frac{\sigma}{\epsilon_0} \mathbf{n} = \mathbf{E}_2^\perp \quad (2.3)$$

where  $\mathbf{n}$  is the unit normal vector from the region of  $\epsilon = \epsilon_1$  to the region of  $\epsilon = \epsilon_2$ . Furthermore the normal field strength *exactly* at the surface, without including the field due to induced charge on that surface ( $\mathbf{E}^\perp$ ), is the average of the normal field strength at an infinitesimal distance from the surface including *all* charges:

$$\mathbf{E}^\perp = \frac{\mathbf{E}_1^\perp + \mathbf{E}_2^\perp}{2} \quad (2.4)$$

The difference between  $\mathbf{E}_1^\perp$  and  $\mathbf{E}_2^\perp$  arises by superposition with the field of the polarization charge at the surface which has a magnitude of  $\sigma/2\epsilon_0$  in both normal directions (Griffiths, 1999b, 17).

Eqs. 2.2–2.4 can be combined into one expression relating the density of induced polarization charge ( $\sigma_i$ ) to the normal field strength on the surface of dielectric boundary element  $i$ :

$$\sigma_i = \frac{2(\epsilon_1 - \epsilon_2)}{\epsilon_1 + \epsilon_2} \epsilon_o \mathbf{E}_i^\perp \quad (2.5)$$

The component of the field strength normal to the tangent plane of the boundary surface element is (Jackson, 1999c, 4):

$$\mathbf{E}_i^\perp = \sum_j \frac{q_j}{4\pi\epsilon_o} \frac{(\mathbf{r}_i - \mathbf{r}_j)}{|\mathbf{r}_i - \mathbf{r}_j|^3} \cdot \mathbf{n}_i \quad (2.6)$$

If charge  $j$  is the charge of a distant surface element, it is treated as a point charge at  $\mathbf{r}_j$ . Otherwise if element  $j$  is a sub-tiled surface element, the expression  $(\mathbf{r}_i - \mathbf{r}_j) \cdot \mathbf{n}_i / |\mathbf{r}_i - \mathbf{r}_j|^3$  in (2.6) is replaced by its weighted average (by subelement area) taken over all subelements of  $j$ . Note that  $q_j$  is the *effective* charge of each entity.

Eqs. 2.1 and 2.5 suffice to compute all initially unknown surface (electrode or dielectric) charges. With these charges known, *all* charges in the system are known. The electric field can then be computed for any location by superposition of the Coulombic fields of individual charges (using appropriate sub-tiling for nearby surface charges).

## 2.2.2 Matrix inversion

My computer code calculates discretely tiled radially symmetric surfaces or, in other words, boundary surfaces of

shapes that can be produced by turning a piece on a lathe, including hollow shapes (cylindrically symmetrical). Techniques for tiling discretely more general surfaces are known and could be used together with my method for solving the electrostatics needed to explore more general geometries than those in this study.

The electrostatic field is long-range — the field strength at all locations depends on all charges. Since the coefficient matrix for those relations is dense, the computational method chosen for solving the linear equations to determine surface charges is LU decomposition (Bowdler et al., 1971, implementation by Whaley and Dongarra, 1997). Inverting an  $N \times N$  matrix by LU decomposition requires order  $N^3$  operations. Fortunately however, the LU decomposition needs to be executed only once for a given surface geometry. If source charges are moved, the electrostatic equations can be solved by repeated back-substitutions using the inverse matrix, requiring order  $N^2$  operations.

### 2.2.3 Gauss box: A control for numerical accuracy

The error from approximating the surface charge distribution as piecewise uniform can be assessed using Gauss’ law. (The approximation requires that the field strength at any point on a surface element equals the field strength measured at the center of charge of the element.) Gauss’ law states that the integral of the electrical flux normal to a closed surface over that closed surface is proportional to the total source charge contained in the enclosed volume (Jackson, 1999d, 39):

$$\oint_{\mathcal{S}} \epsilon \epsilon_0 \mathbf{E} \cdot d\mathbf{a} = \sum_{i \in \mathcal{V}} q_{s,i} \quad (2.7)$$

This conservation law holds for *any* closed surface of *any* shape, and thus applies to any geometry of interest.

Since the density of polarization charge induced by a charge on a dielectric boundary is particularly inhomogeneous when the charge is close to the surface, the local surface region proximate to other charges must be made into smaller discrete surface elements. On the other hand, an excessive number of surface elements is computationally expensive. Since S4 charges move relative to dielectric boundaries in my computer experiments, all S4 positions must be taken into account in designing surface tiling. The adequacy of the surface tiling must be checked for all positions taken

by S4 charges, which can be done by verifying Gauss’ law for each position of the S4. For instance, the sum of all S4 and other source charges contained in the region of protein dielectric in Fig. 2.1 (a) must be accurately recovered by summing the normal field strength multiplied by the permittivity and the element area, over the surface bounding that region ( $\sum_{j \in \mathcal{S}} \epsilon_j \epsilon_0 E_j^\perp a_j = \sum_{i \in \mathcal{V}} q_{s,i}$ , where  $j$  varies over all elements of the closed surface  $\mathcal{S}$  and  $i$  varies over all charges within the volume  $\mathcal{V}$  enclosed by  $\mathcal{S}$ ).

My approach to solving the electrostatics differs from the more common approach of solving Poisson’s equation on a spatial grid. The approach I use (Boda et al., 2004) is based on relations describing boundary conditions (making the method a ‘boundary element method’, BEM). The resulting boundary integral equations are made discrete on a surface grid. Owing to the relatively small number of surface elements compared to the number of volume elements, a full description of the charge distribution and therefore the electric field can be stored in computer volatile memory. From this information any desired electrostatic output variable can be computed. Exhaustive *a posteriori* tests of solution accuracy are possible, such as verification of results by checking the consistency of calculated surface charges against the integral number of charges enclosed using Gauss’ law.

### 2.2.4 Computation of gating charge

S4 charge movements are restricted to a subrange of the distance between the electrodes. The electrodes record a displacement current due to the variations of the electrical field produced at the electrodes by the S4 charges. It is important to assess this charge displacement because the displacement current (and therefore its integral, the charge displacement) can be directly observed in experiments: the displacement charge is the ‘gating charge’.

The electrode charge displaced by the motion of S4 charges is assessed in independent ways to check numerical accuracy. One method directly measures the integral of the displacement that reaches the internal or external electrode. Convenient surfaces for measuring this displacement are the internal and external dielectric boundaries of the membrane and protein. Since the electric field strength perpendicular to these surfaces has already been determined in the computation of induced charge, the electrical fluxes through these surfaces can be computed via integration of the known nor-

mal field strength over the surface area.

A method to solve for charge displacement is provided by the Ramo-Shockley theorem (Shockley, 1938; Ramo, 1939). This method first solves the electric field determining the ‘electrical distance’ of a source charge, which is the field produced by the electrodes in the absence of source charges inside the simulation cell. The gating charge corresponding to an S4 position in a simulation including *all* charges is given by scaling source charges by their respective electrical travel:

$$Q = -\frac{1}{1 \text{ volt}} \sum_j q_j [U(\mathbf{r}'_j) - U(\mathbf{r}''_j)] \quad (2.8)$$

where  $U$  is the potential with all source charges removed and the external electrode fixed at 1 volt; and  $\mathbf{r}'_j$  to  $\mathbf{r}''_j$  are the endpoints of the trajectory of  $q_j$ . This method has been described for simulation cells like the ones used in this study (Nonner et al., 2004). An important implication of this theorem is that the gating charge contributed by an S4 charge is exclusively determined by the position of the S4 charge in the simulated system. It is entirely independent of other source charges, fixed or moving, that exist in the system.

Another implication of the Ramo-Shockley theorem is used in the computation of potential energy (described below in ELECTROSTATIC POTENTIAL ENERGY, SUBSEC. 2.2.5). The Ramo-Shockley theorem implies that applying a voltage to the electrodes modifies the electrical potential at the location of a charge by the fraction of applied voltage corresponding to the electrical distance of that charge ( $U(\mathbf{r}_j)/1 \text{ V}$ ). This is true regardless of the presence of other charges and of dielectrics in the system.

### 2.2.5 Electrostatic potential energy

The charges of the VS move in an electric field that originates from other intrinsic charges, charges induced on dielectric boundaries, and charges delivered from an external battery to the electrodes to establish a voltage clamp (or under natural conditions from the charges that produce the action potential). There are therefore both internal and external sources of electrical work. The biological purpose of the voltage sensor is to transduce electrical work from this environment into mechanical or other work that is applied to other parts of the channel, in particular toward operating the gate of the conducting pore.

The VS can be viewed as traveling in a force field that is probed by fixing the positions of the VS while measuring the

force on the VS, both translational and rotational. Integrating the force along the path of movement gives the required work for moving the VS between the endpoints of the probed path:

$$\Delta W = \sum_s q_s \int_{\mathbf{r}_{s,\text{old}}}^{\mathbf{r}_{s,\text{new}}} \mathbf{E}(\mathbf{r}_s) \cdot d\mathbf{r}_s \quad (2.9)$$

where the summation is over the source charges ( $q_s$ ) moving with the VS, and  $\mathbf{E}$  is the field produced by all charges of the system, excluding  $q_s$  itself. Note that the electrode charge is continually updated by the voltage clamp as the VS moves along the path.

This method of computing work requires that an entire path be scanned at small intervals for a path integral. It is computationally expensive and generates cumulative numerical errors. A more efficient method based on a direct calculation of work is desirable, one that only needs to probe the endpoints of the path. However, I have used the path integration of force as a useful control for other methods that compute work.

A highly efficient method to compute work can be constructed using the Ramo-Shockley theorem. This method requires the computation of the configurational energy when the electrodes are grounded (hence  $V_m = 0$ ) and the charge displacement for a given configuration of source charges. Computation of the charge displacement is described in COMPUTATION OF GATING CHARGE, SUBSEC. 2.2.4, and the method for computing configurational energy when  $V_m = 0$  follows here.

The configurational energy considered in my simulations is the electrostatic energy (including all implicit polarization stress). The configurational energy at a given potential is the interaction energy of every charge in the system with: the source charges; induced dielectric polarization charges (including implicit microscopic stress from polarization); and the charges on the electrodes:

$$W_{\text{config}} = W_s + W_{\text{diel}} + W_{\text{el}} \quad (2.10)$$

where the interaction energy (with all charges) of: source charges is  $W_s$ ; induced charges for dielectrics is  $W_{\text{diel}}$ ; and electrode charges is  $W_{\text{el}}$ .

The configurational energy can also be decomposed into the total electrostatic interaction of all explicit charges in the system plus the implicit mechanical energy of twisting

and stretching the polarized molecules:

$$\begin{aligned} W_{\text{config}} &= W_{\text{electrostatic}} + W_{\text{diel, stress}} \\ &= \frac{1}{2} \sum_j q_j V(\mathbf{r}_j) + W_{\text{diel, stress}} \end{aligned} \quad (2.11)$$

The total electrostatic energy of a discrete charge distribution is  $\frac{1}{2} \sum_j q_j V(\mathbf{r}_j)$ , where  $q_j$  are all the source and induced charges *in vacuo* including dielectric and electrode charges, and  $V(\mathbf{r}_j)$  is the potential due to all charges not located at  $\mathbf{r}_j$  (Griffiths, 1999b). For dielectric polarization charges, the additional mechanical term  $W_{\text{diel, stress}}$  corresponds to the mechanical work of twisting and stretching polarized molecules, including any implicit electric fields involved in these deformations.

The configurational energy when the electrodes are grounded ( $W_{\text{config}}^{V_m=0}$ ) is then:

$$\begin{aligned} W_{\text{config}}^{V_m=0} &= \underbrace{\frac{1}{2} \sum_s q_s V(\mathbf{r}_s)}_{W_s} + \underbrace{\frac{1}{2} \sum_d q_d V(\mathbf{r}_d)}_{W_{\text{diel, electrical}}} + \underbrace{W_{\text{diel, mech}}}_{W_{\text{diel} \equiv 0}} \\ &\quad + \underbrace{\frac{1}{2} \sum_{el} q_{el} V(\mathbf{r}_{el})}_{W_{el=0}} \end{aligned} \quad (2.12)$$

where  $V(\mathbf{r})$  is the potential due to all charges not located at  $\mathbf{r}$ ,  $q_s$  are the source (not effective) point charges,  $q_d$  are all induced polarization charges on dielectric boundaries and surrounding source charges, and  $q_{el}$  are all charges on electrodes. The work to polarize dielectric boundaries is  $W_{\text{diel}} \equiv 0$  since there must be no net electrical and mechanical work on induced charges at equilibrium (Griffiths, 1999c, pg. 193). Additionally, no work is required to place charges at the electrodes ( $W_{el} = 0$ ) when the electrodes are grounded:  $V(\mathbf{r}_{el}) = 0$ .

Therefore, the total configurational energy when the electrodes are grounded is:

$$W_{\text{config}}^{V_m=0} = \frac{1}{2} \sum_s q_s V(\mathbf{r}_i) \quad (2.13)$$

In other words, the total configurational energy is equal to the work to place the source point charges in the potential

field produced by all charges, including those produced by dielectric polarization and charges on the electrodes.

**The Ramo-Shockley based method** used for the efficient computation of electrostatic potential energy is based on the fact that the Ramo-Shockley theorem allows the dissection of the total electrostatic work (including configurational and displacement energies) into two components  $\Delta W_1$  and  $\Delta W_2$ , computed separately as follows (He, 2001):

1. With zero voltage applied to the electrodes, compute the configurational energies for the given old and new positions of the VS charges. If the position of VS charges change in terms of electrical distance between these two geometrical positions, displacement charge flows from one electrode to the other.

Since both electrodes are at the same potential, no work is involved in that charge displacement. Hence,

$$\Delta W_1 = W_{\text{config, new}}^{V_m=0} - W_{\text{config, old}}^{V_m=0} \quad (2.14)$$

2. Apply the desired voltage  $V_m$  between the electrodes. This will modify the potential energy of the VS charges  $q_i$  by

$$\Delta W_2 = -QV_m \quad (2.15)$$

where  $Q$  is the charge displaced at the electrodes when moving from the old to the new position (see Eq. 2.8).

Therefore, the total potential energy change sensed by the VS is:

$$\Delta W = W_{\text{config, new}}^{V_m=0} - W_{\text{config, old}}^{V_m=0} - QV_m \quad (2.16)$$

This work defines the ‘electrostatic potential energy landscape’ in which the VS operates under an applied voltage. Note that the configurational energy only needs to be determined for one applied voltage, 0 mV. Landscapes for any applied voltage can then be computed once the displacement charge for the S4 charge position at that applied voltage is known. The displacement charge itself is efficiently computed using the Ramo-Shockley theorem as described previously (Eq. 2.8). Note that for all graphs, electrostatic potential energy of the VS will be reported relative to the 0 nm translation position (and 0° rotation for potential energy landscapes).



### 2.2.6 Maxwell stress

Charges buried in the protein polarize water in the baths and attract induced polarization charges. The polarization charges are induced on the water surface, and their attraction produces a pressure (normal component of the Maxwell stress) that tends to bring water toward the charges buried in the protein. If a lipid bilayer is uniformly charged to 400 mV, the electrostrictive pressure across the bilayer is about 0.3 MPa (3 atm). This condition typically breaks the bilayer by hypothetically stabilizing the formation and expansion of transmembrane pores (Melikov et al., 2001; Troiano et al., 1998).

The normal component of the Maxwell stress (pressure,  $\mathcal{P}$ ) acting at a dielectric surface is the product of the induced surface charge density ( $\sigma$ ) and the normal component of the electric field at that surface ( $\mathbf{E}^\perp$ ):

$$\mathcal{P} = \sigma \mathbf{E}^\perp \quad (2.17)$$

Both quantities on the right hand side are computed in my electrostatic analysis of the system (Eq. 2.5). Maxwell stress may stabilize or destabilize structures composed of charges embedded in a weak dielectric. Therefore, I assess the strength and distribution of the normal component of Maxwell stress for VS models.

### 2.2.7 Statistical mechanics

A partition function is computed from the electrostatic potential energy. The configuration space has two degrees of freedom in VS motion: rotation and translation. The partition function (“the key principle of statistical mechanics,” Feynman 1988) in discrete configuration space is:

$$\mathcal{Q} = \sum_{i,j} e^{-E_{ij}/k_B T} \quad (2.18)$$

where  $i$  and  $j$  are the indices of the rotational and translational discrete positions;  $E_{ij}$  is the electrostatic potential energy of the VS in configuration  $(i, j)$ ;  $k_B$  is the Boltzmann constant; and  $T$  is absolute temperature.

Movement of S4 charges is restricted in my studies to the rotational range of  $-180^\circ$  to  $+180^\circ$  and a typical translation range of  $-1.925$  nm to  $+1.925$  nm relative to the central position. Each degree of freedom is made discrete in 50 increments resulting in a total of 2500 energy computations for the discrete partition function.

With this partition function known, the probability of a configuration is:

$$P_{ij} = \frac{1}{\mathcal{Q}} e^{-E_{ij}/k_B T} \quad (2.19)$$

and the expectation value of a random variable  $X$  is:

$$\langle X \rangle = \sum_{i,j} X_{ij} P_{ij} = \frac{1}{\mathcal{Q}} \sum_{i,j} X_{ij} e^{-E_{ij}/k_B T} \quad (2.20)$$

The random variables of interest are the rotational and translational positions, the associated gating charge and the Maxwell stress. These are computed for 1 mV steps in the range from -100 mV to +100 mV of membrane voltage.

I also compute the expectation of electrostatic potential energy for the VS at the particular translational positions with rotational equilibrium established at each translational position. The statistical weights are then given by the rotational partition function for that translational position.

## 2.3 Details of the simulation environment

The model comprises a region of inhomogeneous dielectrics surrounded by an eggshell-shaped system of electrodes (Fig. 2.1). The electrode eggshell is composed of three regions: two half-spheres (of radius  $r = 5.0$  nm) interconnected by an open cylinder (of radius  $r = 5.0$  nm and height  $d = 3.0$  nm). The intracellular hemisphere is at a fixed potential  $\psi/2$ , where  $\psi$  is the applied transmembrane voltage; the extracellular hemisphere electrode is anti-symmetrically fixed at  $-\psi/2$ . The cylindrical electrode joining the hemispherical electrodes is subdivided into bands, each of which is held at the potential  $-\psi * z/d$ , where  $z$  is the height of the center of the band relative to the midpoint of the system, and  $d$  is the total length of the cylinder. Therefore the potential on the cylinder varies linearly from  $-\psi/2$  at the junction with the extracellular electrode, to 0 at the midpoint, to  $\psi/2$  at the junction with the intracellular electrode.

The space enclosed by the electrodes is divided into four volumes: the two aqueous baths, the membrane and the protein. The membrane is a disk of the same height as the cylinder electrode (3.0 nm) and has a radius of 5.0 nm. It has a fixed dielectric coefficient  $\epsilon_m = 2$ , representing its lipid composition. The protein region is located in the center of

the simulation environment and spans the membrane (its dielectric is described by a varied dielectric coefficient,  $\epsilon_p$ ); for the paddle model,  $\epsilon_p = \epsilon_m$ . The space between the upper surface of the membrane/protein and the extracellular electrode and the space between the lower surface and the intracellular electrode is an aqueous region with a fixed dielectric coefficient of  $\epsilon_w = 80$ .

For all statistical mechanics calculations, simulation temperature is fixed at 30°C (see eqs. 2.18-2.20).

### 2.3.1 Sliding helix model

Embedded at the center of the membrane is the protein region (of  $\epsilon_p$ ) representing the S4 and the surrounding transmembrane domains;  $\epsilon_p$  is varied by experiment, but for most cases is set at 4. The protein region is radially symmetric, of radius 2.15 nm.

Moving radially inward from the membrane juncture, there is the ‘gating pore’ from 1.966 nm to 1.266 nm. The surface smoothly dips from a depth of  $\pm 1.5$  nm at the juncture with the membrane to the total height of counter charges plus 0.3 nm on either side (between  $\pm 0.6$  nm to  $\pm 0.975$  nm); the S2 and S3 counter-charges are placed equally close to the protein/water interface for all variations. The pore is smoothed by rounded corners of radius 0.15 nm.

At the center is the surface of the S4 proper, of radius 1.266 nm and length 6.5 nm. The  $\alpha$ -helix lies within this envelope. The S4 charges are at a radius of 1.0 nm, each split into 3 charges of  $1/3 e_o$  on a circle of radius 0.122 nm centered around the charge position (Fig. 2.2). This reflects the structure of arginine residues’ guanido group charge distribution. The S4 charges are separated in the  $z$ -direction by 0.45 nm and in the  $xy$ -plane by  $60^\circ$  (each sixth residue completes a full turn counter to the direction of the  $\alpha$ -helix). There are 6 S4 charges, some of which are eliminated or replaced with dipoles in specific computations to simulate charge-neutralization mutants.

Counter-charges are located in the protein dielectric on a curve of 1.4 nm radius, concentric to the curve of the S4 charges. Counter-charges are generally spaced at angular intervals different from those of the S4 charges; the interval

ratios of counter- and S4 charges are referred to by fractions between  $1/2$  and  $3/2$ . There are three counter-charges, centered at the midpoint of the membrane. To simulate experiments with charge neutralization mutants, some of these counter-charges are either eliminated for specific computations or replaced with dipoles.

The relationship of S4 charges and counter-charges for a given translation is given in Fig. 2.4. In figures mapping translation to applied voltage (such as Fig. 3.5 a), the translational axis is labeled in terms of that offset — the distance between the *center* of the S4 charges and the *center* of the model membrane and counter-charges along the translational axis of motion, which is the vertical coordinate in Fig. 2.1.

**Dipole mutants.** To simulate charge neutralization mutants from charged residues to glutamine or asparagine residues, two methods are used: simple elimination of a net charge as described previously or replacement of the charge by a dipole. The dipole is centered at the same position as the center of the original S4 charge or S2 & S3 counter-charge. The orientation of the dipole is radial, with the negatively charged end pointing towards the central ( $z$ ) axis of the simulation setup and the positive end pointing away from the central axis. The charges of the dipole are separated by 0.27 nm and the magnitude of each charge is  $1/2 e_o$  (Pauling, 1960; Lozano-Casal et al., 2008). This dipole representation of the mutant produces favorable interactions not present in the representation by simple charge deletion.

### 2.3.2 Paddle model

In simulations of the ‘paddle’ model, the S4 region is entirely buried in the membrane region with the axis of the helix parallel to the membrane plane. The number of S4 charges is four (as in  $K_vAP$ ). Since the radius of the  $\alpha$ -helix is 1.122 nm, the membrane thickness is extended by 0.5 nm to 3.5 nm, allowing translational motion as well as rotational motion of the S4 helix within the membrane. I explore the range of motion possible without the emergence of the S4 region into the baths.

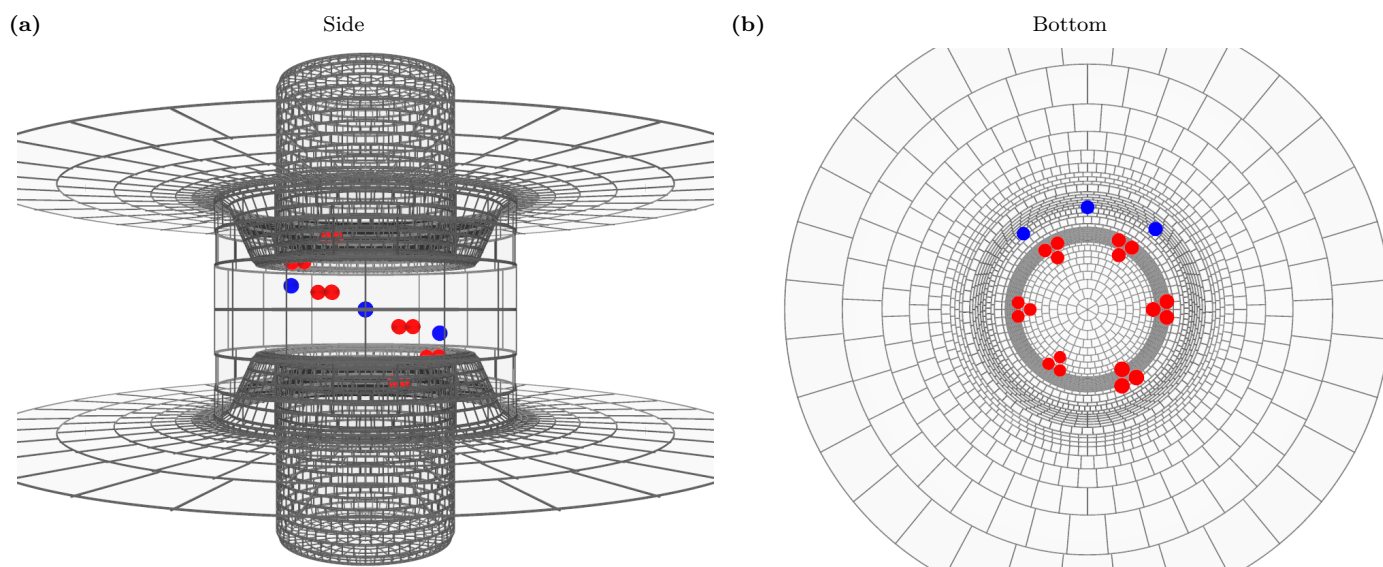


**Figure 2.2: Source charges and dielectric boundaries in a sliding helix model.** The sliding helix bears six triplets of  $1/3 e_0$  point charges (shown as red balls for visibility) representing the guanidinium group of arginine residues. These charges are aligned on a superhelix that is oriented in the direction opposite to that of the S4 helix. The S4 charges are shown at the  $0 \text{ nm}/0^\circ$  position of their translational and rotational dimensions of motion. Counter-charges are  $-1 e_0$  point charges (blue balls). They are aligned in a superhelix concentric with the superhelix of the positive charges (shown for the '2/3' spacing of counter-charges). The dielectric boundaries are shown as a 2D grid; the mesh is a dimensional representation of the surface tiling used in solving the electrostatics (tiling is fine near positions that are close to source charges). The change in average position of the S4 charges under a gradual change of voltage from  $-100 \text{ mV}$  to  $+100 \text{ mV}$  can be seen in the supplementary movies: `tile-helix-side.mp4` [suppl.] & `tile-helix-top.mp4` [suppl.].

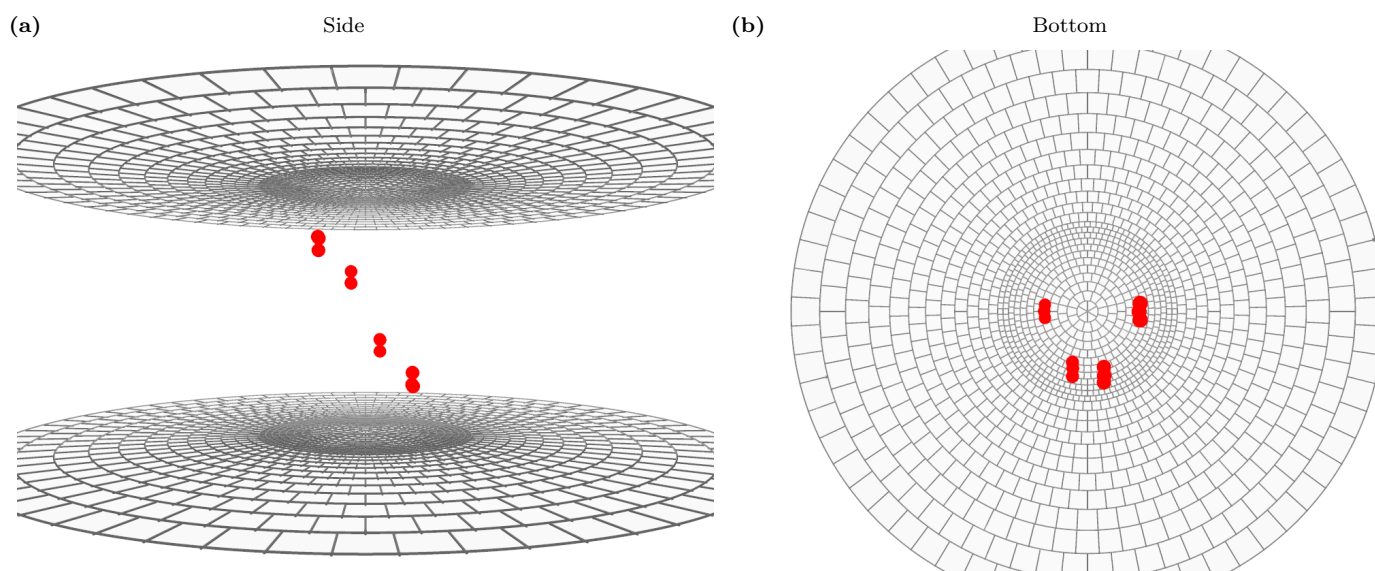


**Figure 2.3: Source charges and dielectric boundaries in a paddle model.** As in the sliding helix of Fig. 2.2, the paddle bears four triplets of  $1/3 e_0$  point charges (shown as red balls for visibility) representing the guanidinium group of arginine residues. These charges are aligned on a superhelix that is oriented in the direction opposite to that of the  $S_4$  helix. The  $S_4$  charges are shown at the  $0 \text{ nm}/0^\circ$  position of their translational and rotational dimensions of motion. The dielectric boundaries are shown as a 2D grid; the mesh is a dimensional representation of the surface tiling used in solving the electrostatics (tiling is fine near positions that are close to source charges). The change in average position of the  $S_4$  charges under a gradual change of voltage from  $-100 \text{ mV}$  to  $+100 \text{ mV}$  can be seen in the supplementary movies: [tile-paddle-side.mp4 \[suppl.\]](#) & [tile-paddle-top.mp4 \[suppl.\]](#).

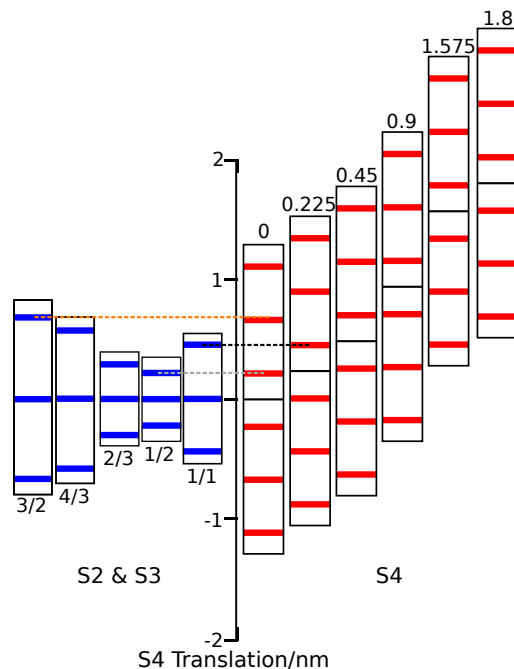


**Figure 2.4: Configurations of S4 charges and counter-charges in sliding helix simulations.** Translational positions of S4 charges are marked in *red* and of counter-charges in *blue*. S4 charges are spaced at a uniform and invariant interval. Counter-charge interval is varied between simulations and is specified by its ratio with the S4 charge interval (labels below the columns). The S4 helix undergoes translation such that its charges line up with counter-charges to varying extents and at varying periods. This is illustrated on the right for a number of S4 positions (translation indicated at the top of columns). The same map applies to the rotational dimension since the rotational intervals between charges are kept in a fixed proportion to the translational intervals ( $60^\circ$  and 0.45 nm respectively for 1/1).

## Chapter 3

# Results and Discussion

Can an electrostatically viable voltage sensor model be constructed on the basis of proposed models? If such a model is at hand, its sensitivity to model parameter variation can be explored in order to understand why the model works. Verifiable predictions can be made about the electrostatic consequences of charge mutants. I will consider three criteria in evaluating VS models:

1. The VS model produces adequate gating charge. For *Shaker*  $K^+$  channels (Jan et al., 1977; Hoshi et al., 1990), a total gating charge movement of  $> 3 e_0$  per channel subunit is expected (Schoppa et al., 1992; Sigg et al., 1994; Aggarwal and MacKinnon, 1996). When the membrane potential changes from a large negative to a large positive value, this charge determines how large the change in electric potential energy is for an individual VS.
2. The model VS moves at the time scale of gating. Since such motion occurs in condensed matter, its rate is limited by friction and possibly energy barriers. Consider the passage of a single  $K^+$  ion across the pore of a  $K^+$  channel: in a large-conductance  $Ca^{2+}$ -activated  $K^+$  channel, a typical passage time is on the order of 30 ns (corresponding to  $\approx 20$  pA conducted by a queue of 3  $K^+$ ). If the VS experiences at least as much friction as the friction in  $K^+$  motion through a channel pore (even though the VS is considerably larger than  $K^+$ ) and the VS completes its motion within 3 ms (Islas and Sigworth, 1999), then it can not encounter electrostatic energy barriers greater than 11.5 kT ( $\approx 0.3$  eV).
3. The model VS provides adequate force for operating parts of the channel molecule constituting the gate of the pore. This force is related to the number of VS

charges that are in the membrane electric field at a given moment. That number of charges is also a determinant of the slope of the gating-charge/voltage (Q/V) relationship. The VS model therefore must predict the slope of the experimental Q/V curve.

My computations simulate an individual, isolated VS. The VS is therefore simulated under ‘zero-load’ conditions: it does not drive the gating machinery that a real VS would drive when integrated in the channel. Since experimental gating currents have been recorded only from whole channels, the VS performance parameters derived from these experiments likely need to be exceeded by a viable VS model studied under zero-load conditions. Specifically, the total charge movement, slope of the Q/V curve and rate of motion are expected to be reduced in a VS operating under its natural load.

In the following simulations, the S4 helix is modeled as a solid body with embedded positive charges which move with two degrees of freedom, translation and rotation about the helix axis. Counter-charges are kept in fixed positions. These constraints are a first step toward understanding the electrostatics of the VS. If the VS is deformed in addition to the translation and rotation of S4, then total gating charge, internal friction, energy barriers and force developed will be affected.

### 3.1 A ‘paddle’ model

In the original version of the paddle model (Lee et al., 2003), the S4 helix was embedded in the membrane lipid (like a paddle in water) and the proposed motion was like the transfer of a large lipophilic ion between the two lipid/water interfaces.

This model has been found electrostatically implausible in a previous computational study because the electrostatic work required to translocate the multiply-charged S4 helix across the weak dielectric of the lipid is very large (Grabe et al., 2004). The original paddle model has been modified since its inception; a recently proposed version (Tao et al., 2010) has gained features of the sliding helix models that I have analyzed and which are described below (A ‘SLIDING HELIX’ MODEL, SEC. 3.2), while losing paddle-like features. This section presents computations of the original paddle model to assess how unfavorable electrostatic features produce unfavorable consequences for the stability and function of a VS design.

I have simulated an S4 helix whose movements are computationally restricted to not extend the helix beyond the boundaries of the lipid membrane. Electrostatic potential energy of the VS (with respect to the central position) is computed while varying the position in two degrees of freedom. The S4 helix is translated between the two membrane boundaries with its axis kept parallel to the boundaries and allowed to rotate fully about its axis. Electrostatic potential energy maps for three different applied membrane voltages are shown in Fig. 3.1 (a-c), with energy represented in false color. Note that these energy maps are similar for all applied voltages, as if applied voltage has a relatively small effect relative to the contributions of other simulation parameters.

Panel (d) of Fig. 3.1 displays the mean electrostatic potential energy of the VS as a function of translation. This energy is computed by averaging over all rotational angles of the paddle using the statistical weights of the rotational partition function (see STATISTICAL MECHANICS, SUBSEC. 2.2.7). In other words, the energy for each angle is used in a Boltzmann factor to statistically weigh that energy to derive an overall expectation energy for that translational position; graphically, one point for a curve at specific potential in panel (d) is the expectation value calculated from the matching column (by translation) of the respective potential energy graph of panels (a-c).

The energy in (d) has a large maximum when the S4 axis is in the center of the membrane, more than 0.5 eV above the energy at the extreme points of the scanned range of translation (Grabe et al. 2004 scanned a wider range of translation and obtained an even larger variation of energy). The

variation of electrostatic potential energy due to the varied applied membrane voltage are indeed small compared to the large electrostatic barrier. The energy profile makes this VS in essence a bistable structure. When in one extreme position, the S4 is very unlikely to ever flip to the other position.

My energy computations with this paddle model also reveal that translating the helix produces strong rotational forces. At the end points of the  $\pm 0.5$  nm translations from the center, electrostatic potential energy of the VS is minimal in different rotational positions. This applies for all tested membrane voltages. The differences between favorable and unfavorable rotational positions approach 1 eV, making it highly unlikely that the S4 segment could undergo translation without rolling by about half a turn. A proposed model in which the S4 helix moves by translation alone would produce energetically unstable configurations. If the helix is allowed to follow electrostatic force in the rotational degree of freedom, the electrostatics of this paddle model antagonize VS function (Fig. 3.1 d).

Lipid bilayers tend to break down when voltages larger than 400 mV are applied (Melikov et al., 2001; Troiano et al., 1998). The electrostrictive pressure across the bilayer under those conditions is  $\approx 0.3$  MPa (3 atm). In the paddle model, electrical charges are located inside the lipid membrane and create strong electric fields. These fields polarize the water adjacent to the membrane, inducing charge at the lipid/water boundaries. S4 and induced charges attract one another; therefore, the lipid/water boundaries are attracted toward the S4 charges. This is the Maxwell stress. I have computed Maxwell stress on the lipid/water interface (see MAXWELL STRESS, SUBSEC. 2.2.6) to see how this stress relates to the electrostrictive pressure known to break lipid bilayers. For this paddle model, the Maxwell stress on membrane boundary regions near the S4 charges is very large. Fig. 3.2 shows the pressure distributions on the internal and external bath boundaries with a logarithmic false-color scale (pressures range from  $10^2$  Pa in blue to  $2.5 \times 10^8$  Pa in red). The peak pressure on the bath boundaries is much larger than a safe electrostrictive stress, even if the S4 axis is centered in the membrane (the minimal Maxwell stress configuration). The likely consequence of the large Maxwell stresses of the paddle model is that the lipid retreats and thus exposes the charged surface of the helix to both baths. Such a configuration would not function as voltage sensor.

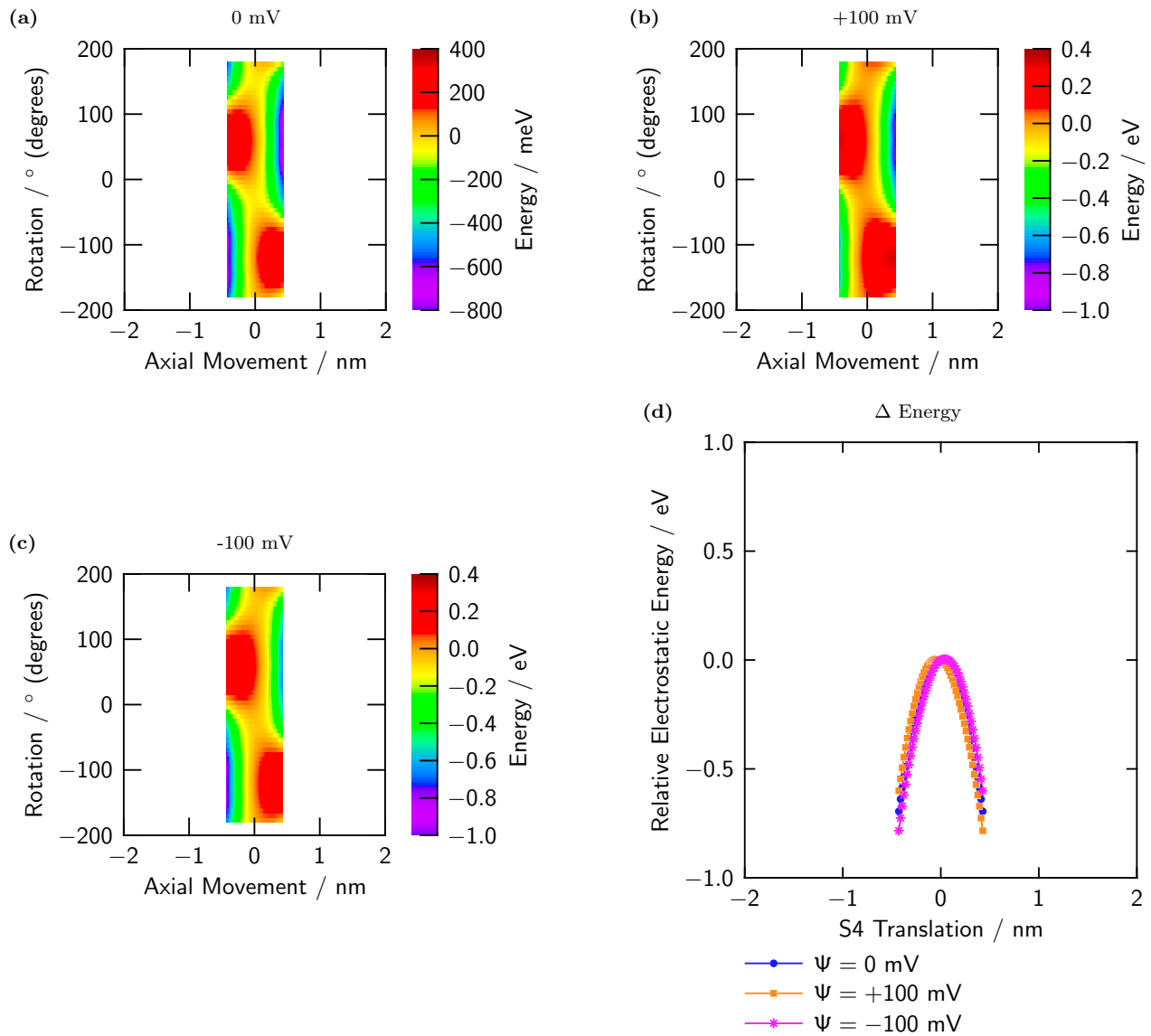


**Figure 3.1: A paddle configuration is electrostatically bistable.** Panels (a-c): false-color maps of electrostatic potential energy of the VS scanned over two degrees of freedom for three applied voltages. The S4 helix axis is parallel to the membrane plane and translated in the direction normal to the membrane plane. The S4 segment is buried in the lipid in all scanned translational positions. Rotation is about the S4 axis. Electrostatic potential energy strongly favors positions near the bath interfaces at all applied voltages. Panel (d): Rotation-averaged electrostatic potential energy versus translation for three applied voltages (averaging is based on the rotational partition function). Since electrostatic potential energy depends on rotational position (panel a), allowing the S4 helix to rotate minimizes energy. Nevertheless, the profile of averaged energy is parabolic, and applied membrane voltage does not remove the large barrier to S4 translation. Note that panels (a-c) show the electrostatic potential energy of the VS relative to that at translation 0 nm and rotation  $0^\circ$  of that graph (Eq. 2.16), while panel (d) shows electrostatic potential energy of the VS relative to translation 0 nm (expectation over the rotational degree of freedom).



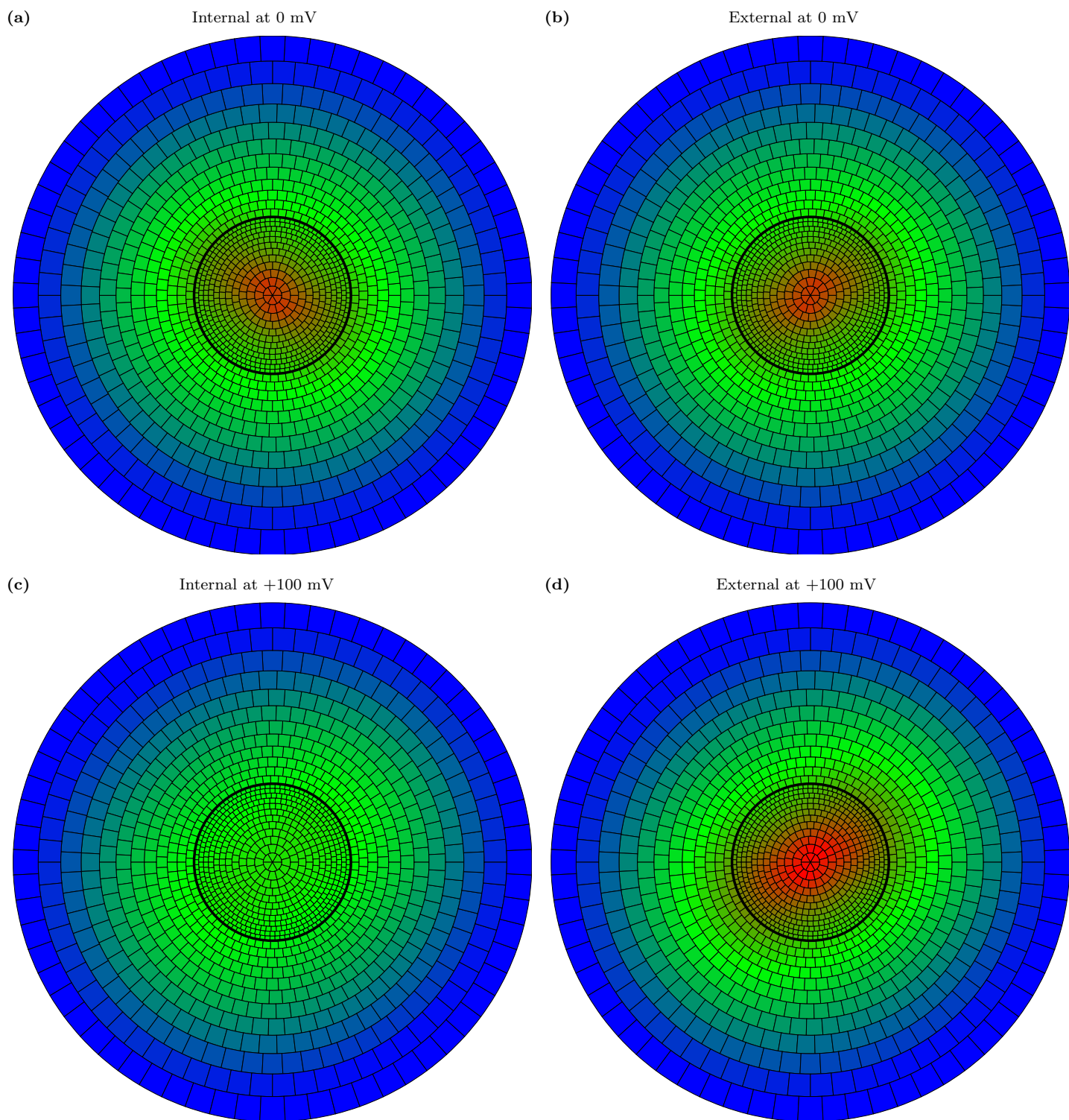


**Figure 3.2: A paddle configuration is mechanically unstable.** False-color maps of the Maxwell stress acting on the water/lipid interfaces. This stress tends to pull the water boundary toward the S4 charges. Logarithmic color scale goes from  $10^2$  Pa (*blue*) through  $10^5$  Pa (*green*) to  $2.5 \times 10^8$  Pa (*red*). The surface area shown is 10 nm in diameter. (An electrostrictive pressure of  $\approx 3 \times 10^5$  Pa is known to break a lipid bilayer.) The position in the membrane of the S4 segment is controlled by the applied membrane voltage (0 or +100 mV), and the Maxwell stress shown is the expectation of the Maxwell stress (based on the translational/rotational partition function). A supplementary movie (`flat-paddle.mp4` [suppl.]) shows how Maxwell stress varies as applied voltage is varied between -100 and +100 mV.

## 3.2 A ‘sliding helix’ model

The sliding helix models investigated here are VS models in which the axis of the S4 helix is oriented perpendicularly to the plane of the membrane. Two independent kinds of motion are allowed: translation along the axis of the S4 helix and rotation about the axis. No particular trajectory in these degrees of freedom is prescribed. Thus both motions envisaged for the ‘helical screw’ hypothesis of S4 motion are possible but are not *a priori* coupled to one another as the term ‘screw’ would imply. A concentric invagination of the protein dielectric around the S4 helix forms a ‘gating pore’. In addition to the S4 positive charges, three negative point charges are present in the protein domain. For the specific version of the sliding helix that I consider in this section, these are aligned in a spiral pattern concentric to that of the S4 charges, but the angular and translational intervals between the counter-charges are chosen to be two-thirds ( $2/3$ ) that of the S4 charge interval (i.e.,  $40^\circ$  and  $0.3$  nm). The counter-charge positions are fixed. The dielectric of the protein is represented by a dielectric coefficient of 4. These parameters have been chosen via an iterative process to identify the envelope of parameters that are physically reasonable and consonant with known biology.

The landscape of electrostatic potential energy (Fig. 3.3) is very different from that computed for the paddle model. When a membrane voltage of  $0$  mV is applied, a trough of electrostatic potential energy tends to confine the S4 charges to a range of positions which can be reached by moving the S4 helix like a screw (Fig. 3.3 a). Thus the S4 segment in this model tends to be electrostatically stable in its environment (rather than being strongly driven towards the baths, like the paddle considered before). The energy trough is quite shallow however, so additional stabilizing features are required to ensure long-term stability.

The bottom of the energy trough is nearly flat, allowing the helical screw to visit a wide range of positions with nearly uniform probability. When a strong positive or negative voltage is applied to the membrane, the energy trough is shortened to a deep pit at either end of the S4 range of screw motion (Figs. 3.3 b & c). Panel (d) shows the expected electrostatic potential energy for each translational position (a statistical average over the rotational degree of freedom based on the rotational partition function, see STATISTICAL MECHANICS, SUBSEC. 2.2.7). There are no significant energy barriers to translation. The applied membrane voltage simply tilts the flat bottom of the energy trough. Altogether, the

electrostatic energetics of this model are consistent with a screw motion — the rotation is a physical consequence of the electrostatics. This voltage sensor strongly resists either exclusively translational or exclusively rotational motion.

As I do for the paddle model, I assess the mechanical stability of the dielectric geometry of the sliding helix model using the computed Maxwell stress. Fig. 3.4 shows the pressure distribution on the protein/water interface (note that the invaginated interface has been mapped onto a plane, see figure legend). Both the intra- and extracellular pressure distributions are shown for a simulation with applied voltages of  $0$  mV or  $+100$  mV.

The Maxwell stress for the sliding helix model is largest where charges are close to the bath interface. Large stresses appear at the water interfaces of the S4 helix where charges face a bath. These stresses do not compromise mechanical stability since the charged groups are in direct contact with water. The surface region lining the gating pore receives a moderate Maxwell stress, except for one angular region located at the bottom of the gating pore close to the innermost and outermost counter-charges (the gating pore is located between the white and yellow rings in Fig. 3.4). There, local Maxwell stress is on the order of  $10^8$  Pa. This magnitude of stress provides a physical cause for the invagination of the water boundary into a nano-scale gating pore, which requires work against the surface tension of the water/protein interface. The existence of a gating pore is thus made plausible by the electrostatics, although the gating pore postulated in the model is not a computed consequence of the physics at this level of modeling. The Maxwell stress due to the near-surface counter-charge is narrowly localized so that it, by itself, would not produce a full-circular gating pore like that assumed in the model. On the other hand, S4 gating charges could help stabilize a larger gating pore on the side(s) where they are exposed.

Since this particular sliding helix model has desirable properties, I compute the partition function over the rotational and translational degrees of freedom for stepwise varied applied voltages. The expectation values of rotational and translational positions and of the predicted gating charge can thereby be determined as functions of voltage. The relationship between displaced gating charge and voltage is a prediction of the gating charge per VS displaced when a voltage is applied to an ensemble of channels in an experiment.

Figs. 3.5 (a) & (b) show the expectation of position for the model VS at given voltages. The positions follow the trajec-

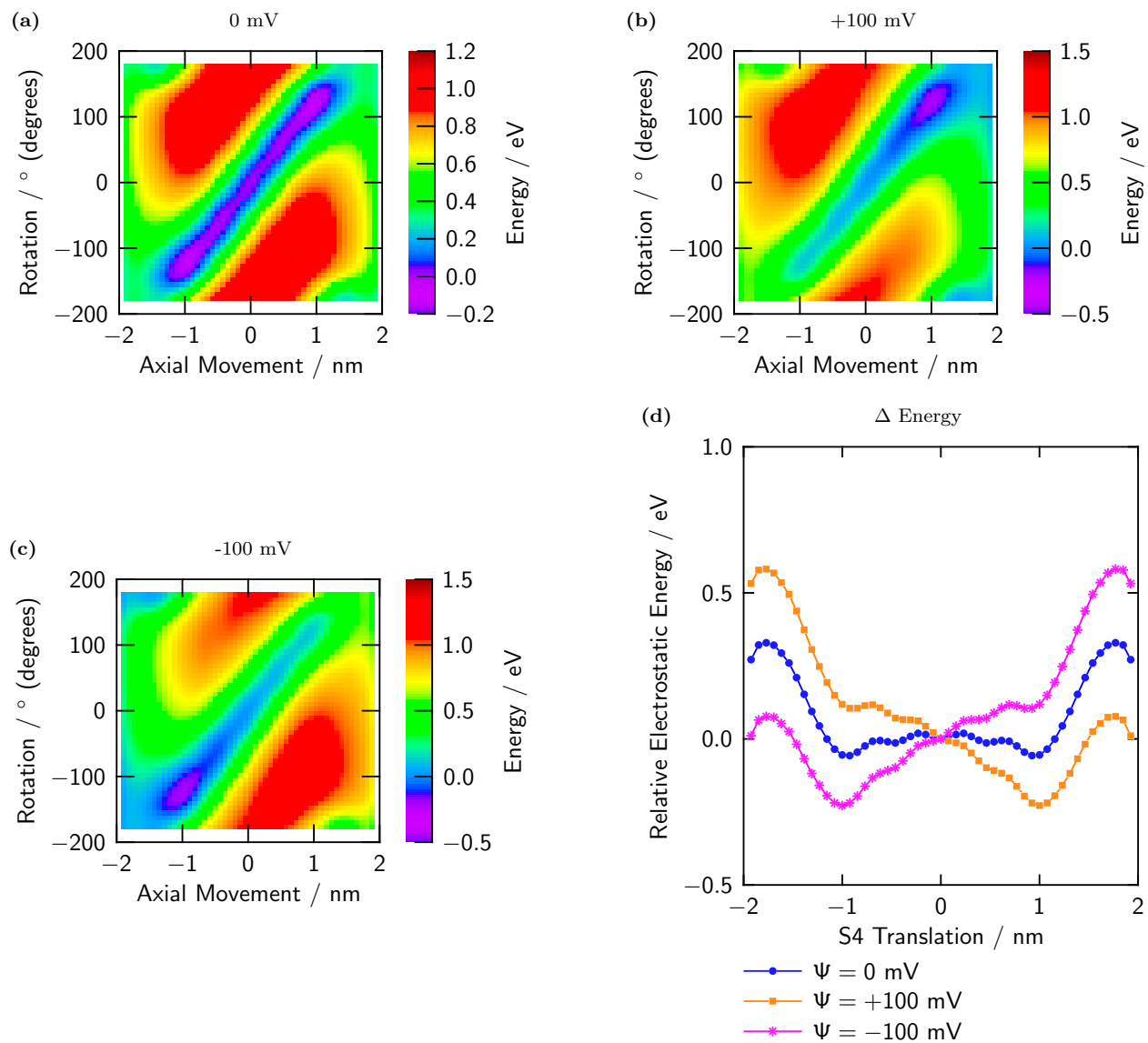


**Figure 3.3: A sliding helix configuration has electrostatics suited for a VS.** Panels (a-c): false-color maps of electrostatic potential energy of the VS scanned over two degrees of freedom, for three applied voltages. The S4 helix has 6 positive charges, the three counter-charges are spaced at the  $2/3$  interval, and the protein dielectric coefficient is 4. The electrostatic potential energy map for 0 mV applied voltage forms a trough favorable to combined translational/rotational ('screw') motion of the S4 helix. Applied voltages of -100 or +100 mV convert the energy trough into a pit at one end of the trough seen with 0 mV. Panel (d): Rotation-averaged electrostatic potential energy versus translation for three applied voltages (averaging is based on the rotational partition function). Since electrostatic potential energy depends on rotational position (panel a), allowing the S4 helix to rotate minimizes energy. The averaged energy forms a trough that tends to restrict translation at both ends but is almost flat over intermediate translations (thus allowing diffusive motion of the S4 helix). Applied voltage tilts this profile (promoting drift/diffusion of the S4 helix). Note that panels (a-c) show the potential energy of the VS relative to translation 0 nm and rotation  $0^\circ$ , while panel (d) shows the potential energy of the VS relative to translation 0 nm (expectation over the rotational degree of freedom).

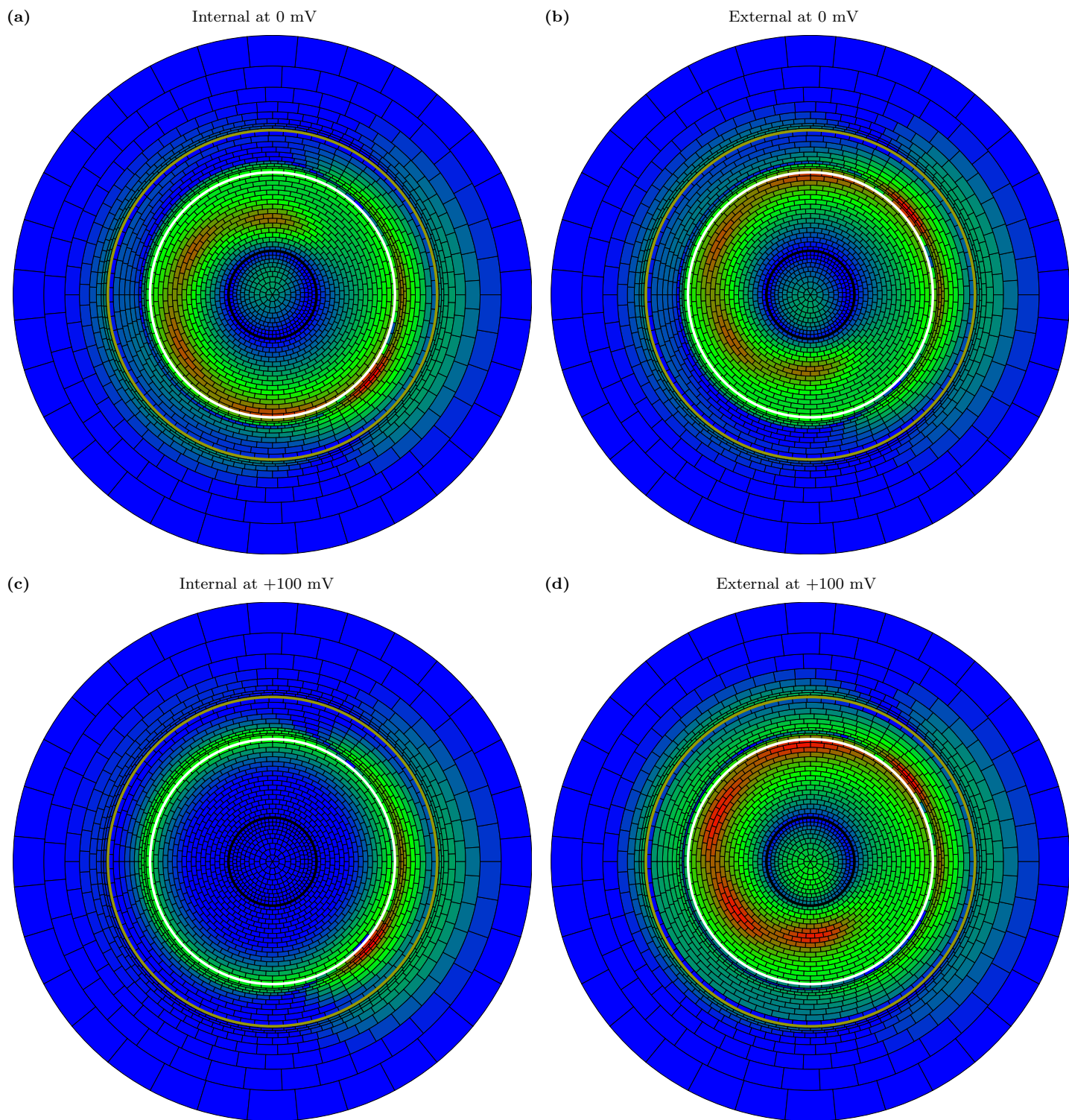


**Figure 3.4: A sliding helix configuration is mechanically stable.** False-color maps of the Maxwell stress acting on the bath interfaces. The gating pore lies between the *yellow* and *white* rings; the top of the S4 segment is delimited by the *black* ring. The Maxwell stress tends to pull the water boundary toward the S4 charges. Logarithmic color scale from  $10^2$  Pa (*blue*) through  $10^5$  Pa (*green*) to  $2.5 \times 10^8$  Pa (*red*). The curved surface of the membrane/protein bath interface (10 nm in diameter) is projected into a plane (preserving path length in walking from the center to the periphery). High pressures occur where charges face water and in locations at the bottom of the gating pore (stabilizing the gating pore near buried counter-charges). The same model parameters are used as in Fig. 3.3. The position in the membrane of the S4 segment is controlled by the applied membrane voltage (0 or +100 mV), and the Maxwell stress shown is the expectation of the Maxwell stress (based on the translational/rotational partition function). A supplementary movie (`f1at-s4.mp4` [suppl.]) shows how Maxwell stress varies as applied voltage is varied between -100 and +100 mV.

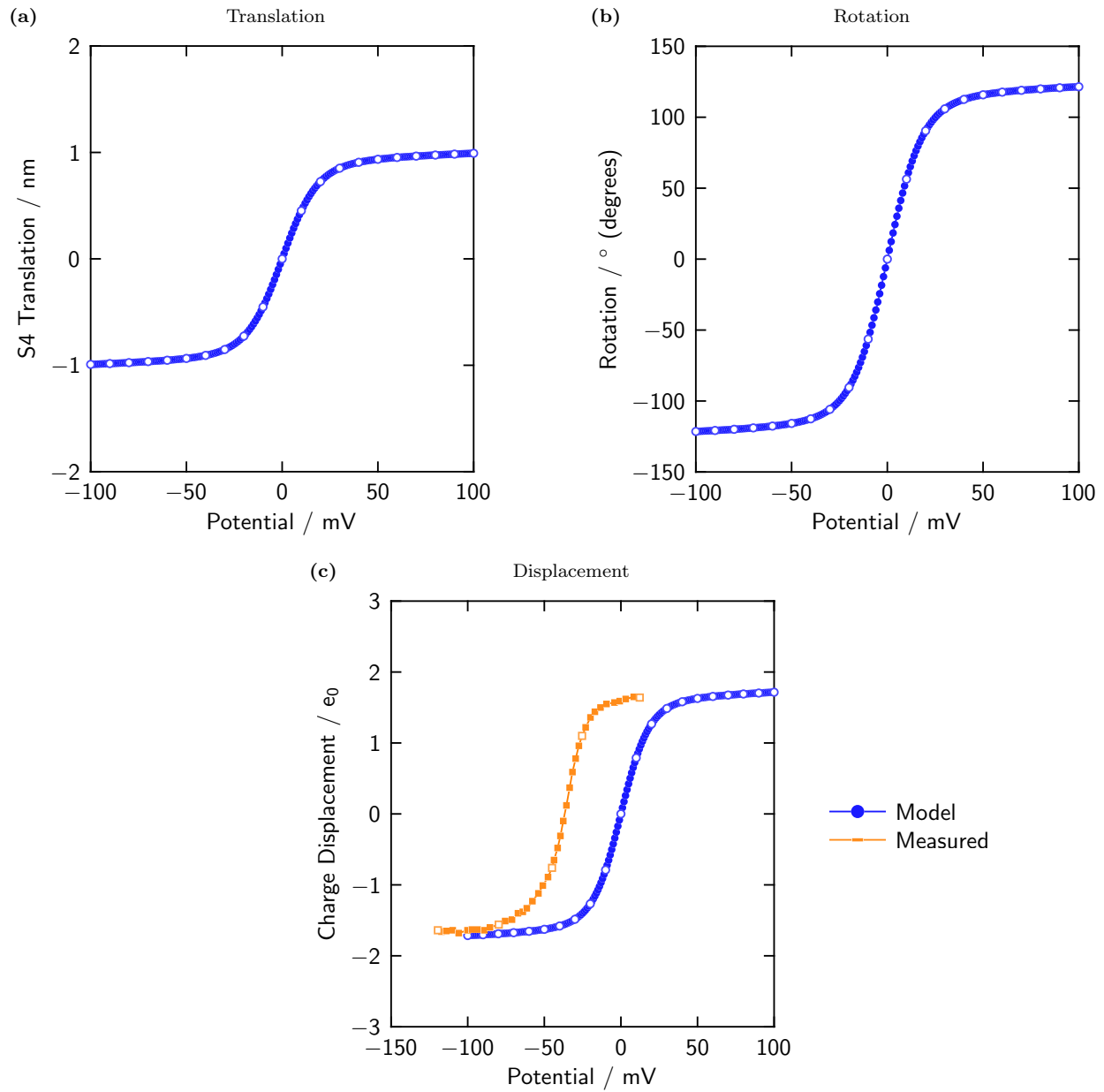


**Figure 3.5: The action of voltage on a sliding helix VS:** Expectations of translation (a), rotation (b) and displaced gating charge (c) in response to varied applied voltage. The expectations of these random variables are computed using the electrostatic partition function for the two degrees of freedom. The same parameters for the sliding helix model are used as in Fig. 3.3. Voltage moves the mean position of the VS in a screw-like trajectory and displaces gating charge of the proper magnitude with the proper slope (an experimental charge/voltage curve (Seoh et al., 1996) for *Shaker*  $K_V$  channels is shown as the orange line in panel c).



tory of a screw motion. Varying the voltage gradually from -100 mV to +100 mV drives the expected position of the VS over the range suggested by the potential energy landscapes in Fig. 3.3. The amount of gating charge displaced over that range of motion (Fig. 3.5 c, blue line) exceeds  $3 e_0$  per VS, which is close to the total gating charge measured per VS in *Shaker*  $K^+$  channels (orange line). Since a VS driving coupled gating machinery might have a smaller range of motion, it is reasonable to expect a model of an uncoupled VS to produce at least as much charge per VS as that observed in channels.

Charge is displaced in the model over a voltage range symmetrical with respect to 0 mV of applied voltage, whereas the experimental charge displacement is centered about a negative voltage. The slopes of the two charge displacement curves are quite similar; the chief difference between the model VS and the real VS is an offset between the charge/voltage curves. The real VS is integrated into a channel and drives the activation gating of the channel. My model voltage sensor is isolated and drives no load. If the voltage offset between the two charge/voltage relations is due to the gating work that the real voltage sensor does on the rest of the channel, then: (1) the gating work is applied in closing the channel, and (2) the counter-force exerted by the gate onto the VS is approximately constant over the range of VS travel (in contrast to an elastic counter-force).

The sliding helix model presented fulfills the criteria for a viable VS model as listed above. Therefore in this study I will use those model parameters as a basis of further exploration of VS electrostatics.

### 3.3 Which model features are important for voltage-sensing by a sliding helix?

Sliding helix models have many features that can be parametrized and studied: counter-charge position & number, protein dielectric, gating pore size & shape and membrane thickness, for example. In this section I present three features of interest that show sensitivity and a significant effect on VS function. In particular, the existence of counter-charges, their spacing and the local dielectric through which they interact with S4 charges are strong determinants of the viability of a VS model.

#### 3.3.1 Counter-charges eliminate the induced-charge barrier

The gating pore reduces the length of the S4 segment exposed to the weak dielectric separating the two baths. The sliding helix model studied in the previous section also includes three negative counter-charges in the region of weak dielectric. Either feature is expected to reduce the energetic cost of moving the S4 charges from the baths into the region of weak dielectric. The role of the counter-charges can be assessed by deleting them from the model. Fig. 3.6 shows electrostatic potential energy of the VS versus translation for the models with and without three counter-charges. Removing the counter-charges produces a large electrostatic barrier, much like that computed for the paddle model described above (Fig. 3.1 d, note the distinct shape in the mid-range, however).

The S4 charges of the sliding helix model induce a substantial charge on the bath interfaces. The induced charges are negative, attracting the S4 charges toward the baths and thereby destabilizing the buried S4 charges. With the buried positive S4 charges neutralized by negative counter-charges, the charges induced on the bath interfaces are greatly reduced, creating a trough of electrostatic potential energy. These computations indicate that an appropriate number of counter-charges are required if the sliding helix model is to function as a VS. The gating pore alone does not lower the induced-charge barrier to the extent needed for the sliding helix models to function as a VS.

Another consequence of the deletion of all counter-charges from the model is that all rotational positions now have equal electrostatic potential energy. Thus the S4 segment in the model no longer operates like a screw. If the delivery of torque is important for operating the gate of the real channel, this would add another consequence to neutralizing mutations of VS counter-charges.

#### 3.3.2 Counter-charge spacing matters

The counter-charges of the described sliding helix models are arranged following the spiral curve on which the S4 charges are positioned. The intervals of the S4 and counter-charges, however, differed for the previously described model (COUNTER-CHARGES ELIMINATE THE INDUCED-CHARGE BARRIER, SUB-SEC. 3.3.1): there, the counter-charges were spaced at  $2/3$  the interval between S4 charges. This precludes simultaneous alignments of more than one S4 charge with a counter-

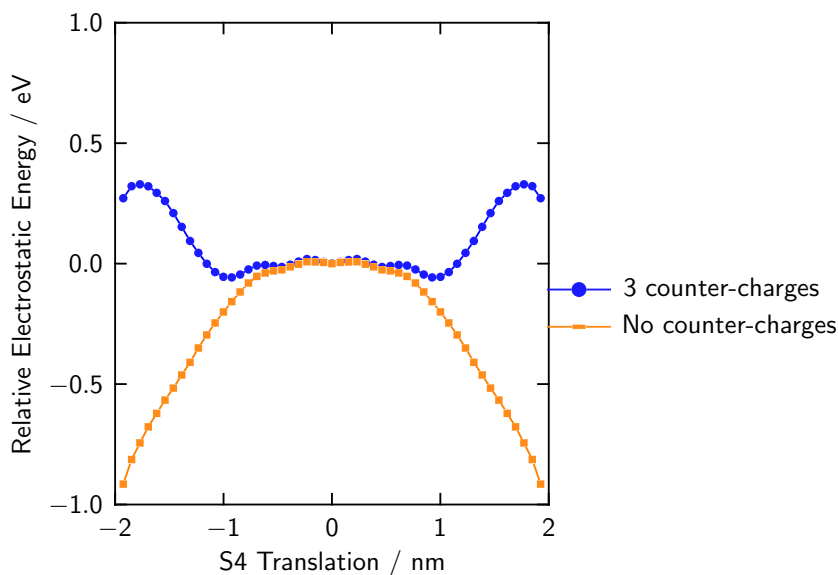


**Figure 3.6: Counter-charges are required for a sliding helix to function as VS.** Electrostatic potential energy of the VS averaged over rotation and relative to that at translation zero versus translation. The *blue* line describes the sliding helix model of Fig. 3.3 which includes three counter-charges. The *orange* line describes the same model but with all counter-charges deleted. The energy profile then becomes parabolic like that of a paddle model (compare Fig. 3.1 d).

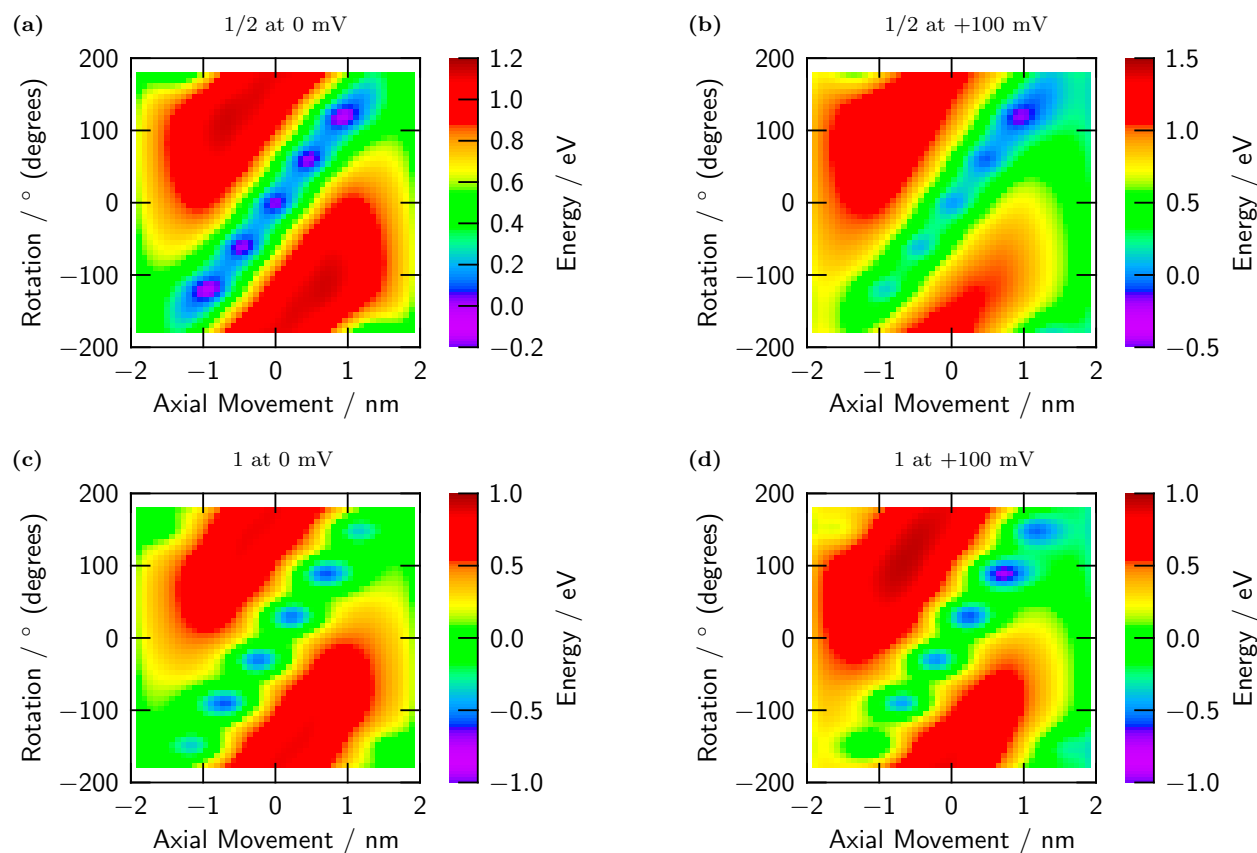
charge (see Fig. 2.4). In order to see how much the close-range electrostatic interactions of charge and counter-charge affect electrostatic potential energy of the VS, I have computed the consequences of counter-charge intervals of  $1/2$ ,  $1/1$ ,  $4/3$ , and  $3/2$  times the interval of S4 charges. A later section (CHARGE MUTATIONS, SEC. 3.4) will present computations of less regular charge spacings obtained by deleting charges at certain positions of a periodic pattern.

Fig. 3.7 shows maps of electrostatic potential energy in the translational and rotational degrees of freedom, for both 0 mV and +100 mV applied voltage. The potential energy of the VS expected when rotation is free is plotted versus translation in Fig. 3.8 with 0 mV curves for different spacings superimposed. The  $1/2$ ,  $1/1$ , and  $3/2$  intervals yield energy landscapes more hilly than those of the  $2/3$  or  $4/3$  intervals; the S4 segment of these models with counter-charges spaced at  $1/2$ ,  $1/1$  or  $3/2$  intervals tend to dwell in more discrete positions in energy valleys. When a strong voltage of +100 mV is applied in these models, some of the energy valleys persist as discrete features.

What are the consequences of these different potential energy landscapes for the gating charge displaced in response

to applied voltage? How does the expected position of the S4 region respond to voltage? Fig. 3.9 shows the expectation translation (a), rotation (b) and charge/voltage relation (c) based on the partition function over rotational and translational degrees of freedom. The charge voltage relations vary in steepness and total displaced gating charge even though the numbers of S4 charges and counter-charges are fixed, as is the dielectric environment. These variations of the charge/voltage curve must originate from the range of travel produced by the applied voltage as well as the distribution of S4 positions among more or less discrete locations. Predicting these variations requires numerical analysis of the electrostatics.

The expectation values for rotation and translation at different voltages (Figs. 3.9 a & b) reveal a monotonic increase in translation as voltage is increased; however, non-monotonic variations of rotation occur in some cases. Thus, for the  $3/2$  counter-charge interval, the rotation is in the opposite direction to that seen for other intervals. Translational motion (and ability to produce translational force) is robust, while rotational motion (and ability to produce torque) is sensitive to counter-charge alignment. Never-



**Figure 3.7: Counter-charge spacing controls electrostatic potential energy landscape (Pt. 1).** The spacing is specified as the ratio of counter-charge spacing to S4 charge spacing (the ratio applies to both the rotational and translational spacing). The protein dielectric coefficient is 4. Energy of each configuration is represented relative to translation 0 nm, rotation 0°. Note differences in scale.

**Figure Continued in Pt. 2.**

theless, the S4 segment is expected to rotate for all tested counter-charge intervals.

Varying a single parameter of counter-charge configuration has strong effects on function in these sliding helix vs models. Counter-charges and their arrangement are crucial for building a working VS.

### 3.3.3 Electrical polarizability of the protein controls effective gating charge

Simulations were conducted in which the dielectric coefficient of the protein region (including the S4 segment) was

varied over the values 2, 4, 8 and 16. Landscapes of electrostatic potential energy for dielectric coefficients 2, 8 and 16 are shown in Fig. 3.10; the potential energy landscape for a dielectric coefficient of 4 was presented in Fig. 3.3. The general effect of increasing the dielectric coefficient is to moderate energy variations. Broader ranges of rotation and translation become accessible (note the varying energy scales between these graphs).

The expectation values of energy (based on the rotational partition function) are shown versus translation in Fig. 3.11. As the dielectric coefficient is decreased, the shallow trough of energy becomes deeper and a pattern of wells and barri-



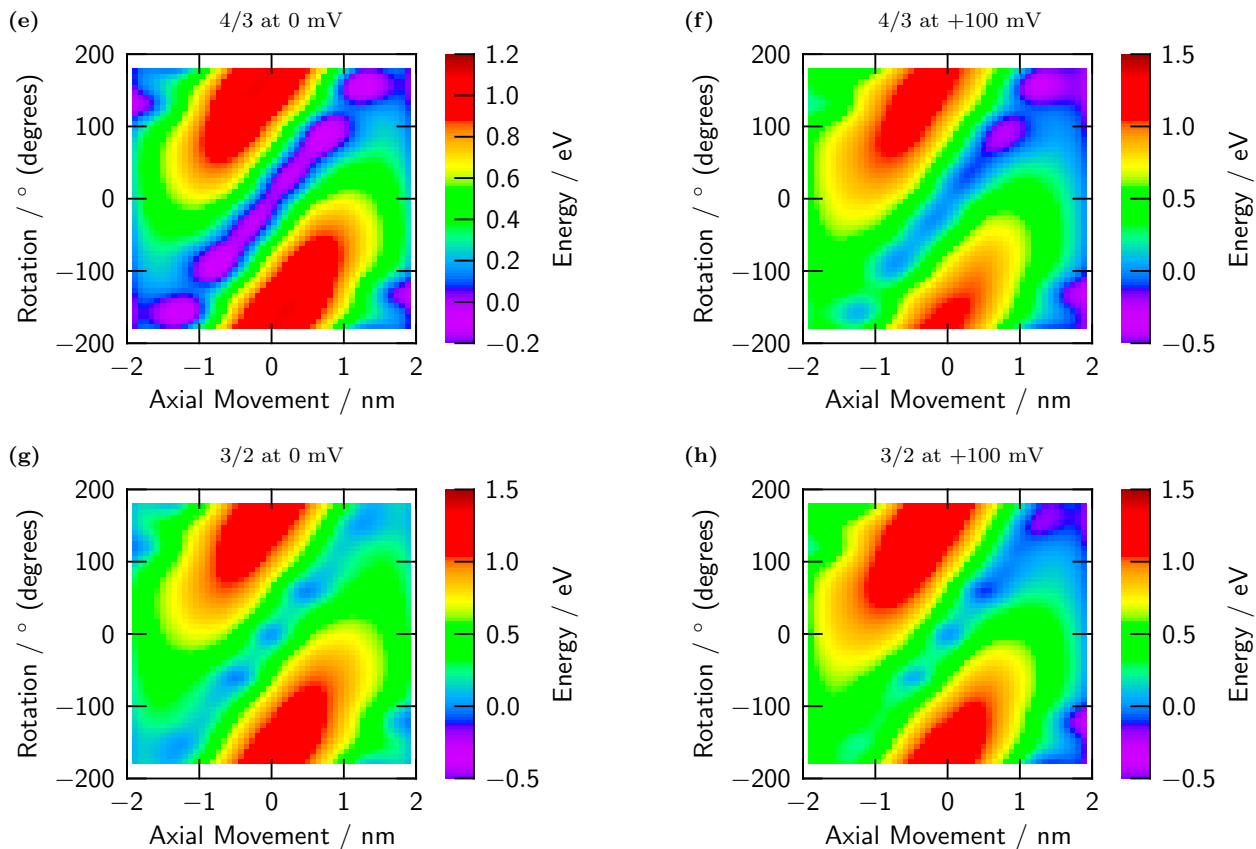


**Figure 3.7: Counter-charge spacing controls electrostatic potential energy landscape (Pt. 2).**

**Figure continued from Pt. 1.**

ers emerges. In particular, significant wells develop around  $\pm 1$  nm of translation.

The changes in potential energy landscape have interesting consequences for the relation between charge displacement and voltage (Fig. 3.12). Reduction of the protein dielectric coefficient increases the slope of the charge/voltage relation. These simulations were all calculated with the same dielectric geometry, protein charges and counter-charges in the model. Nevertheless, the ‘effective gating charge’ of the VS as assessed by the steepness at the midpoint of the charge/voltage curve increases as the protein dielectric coefficient is reduced. The reason for this effect of the dielectric coefficient is evident in Fig. 3.11. With a dielectric coefficient of 2, there are two crisp energy minima at translations

$\pm 1$  nm, leading the S4 segment to dwell preferentially near these two positions. With a dielectric coefficient of 16, however, there is no significant energy variation (at 0 mV) at any position within the energy trough, so that no S4 position is preferred. Hence, the distribution of the S4 segment in the translational degree of freedom varies from a virtual ‘two-state Boltzmann distribution’ to a distribution within a space of uniform potential energy. The uniform-energy distribution of charge approaches hyperbolic rather than exponential asymptotic behavior at extreme voltages. The midpoint slopes of the charge/voltage curves can be analytically determined; the midpoint slope of the charge/voltage curve is three times greater for the two-state case than for the uniform-energy case (Neumcke et al., 1978). In this man-

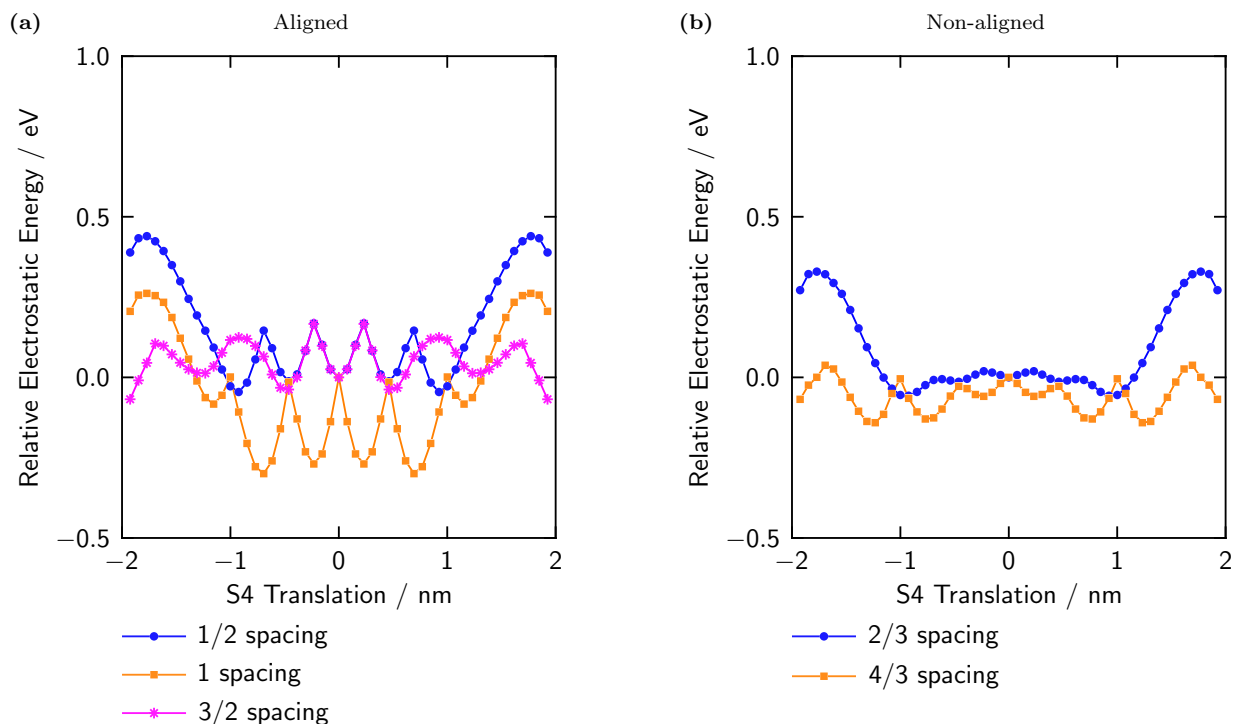


**Figure 3.8: Counter-charge alignment with S4 charges creates electrostatic barriers and wells.** Electrostatic potential energy of the VS versus translation, averaged over rotation and relative to translation 0 nm. The spacing of counter-charges is varied. The protein dielectric coefficient is 4. The spacings of 1/2, 1/1, and 3/2 allow two counter-charges to align with corresponding S4 charges in certain positions, thereby generating ripples of electrostatic potential energy (panel a). The spacings that allow only one counter-charge to align at a time with an S4 charge produce smoother profiles of energy (panel b).

ner, the same structural charges produce up to a three-fold varying effective gating charge as the protein dielectric coefficient (and therefore the potential energy landscape) is varied. The force that can be delivered by S4 charge movement is therefore constrained by the local dielectric coefficient.

### 3.4 Charge mutations act via charge/counter-charge interactions

Seoh et al. (1996) reported the results of 9 neutralization mutants (over 8 residues) of *Shaker* K<sup>+</sup> channels plus the wild-type in terms of open probability and charge displacement per channel. In single mutants, one of the four outer S4 posi-

tive residues or one of three negative charges on the S2 and S3 transmembrane segments were neutralized. In addition, two double mutants were investigated. These mutations produce a complex pattern of change in the charge/voltage curves, including reductions of total gating charge, shift, and alteration of slope and shape. Predicting such patterns is a challenge for a physical model.

For these comparisons, I use 3 counter-charges set at a 2/3 interval to test whether the apparent VS-like behavior of that model as investigated above responds like a biological VS to physiological extremes. The positions of these counter-charges in the biological VS is ambiguous. Unlike S4 charges which are regularly arrayed on a single transmembrane domain that is  $\alpha$ -helical in nature, counter-charges are irregularly placed on multiple helices connected by amorphous linking regions and arranged at various orientations

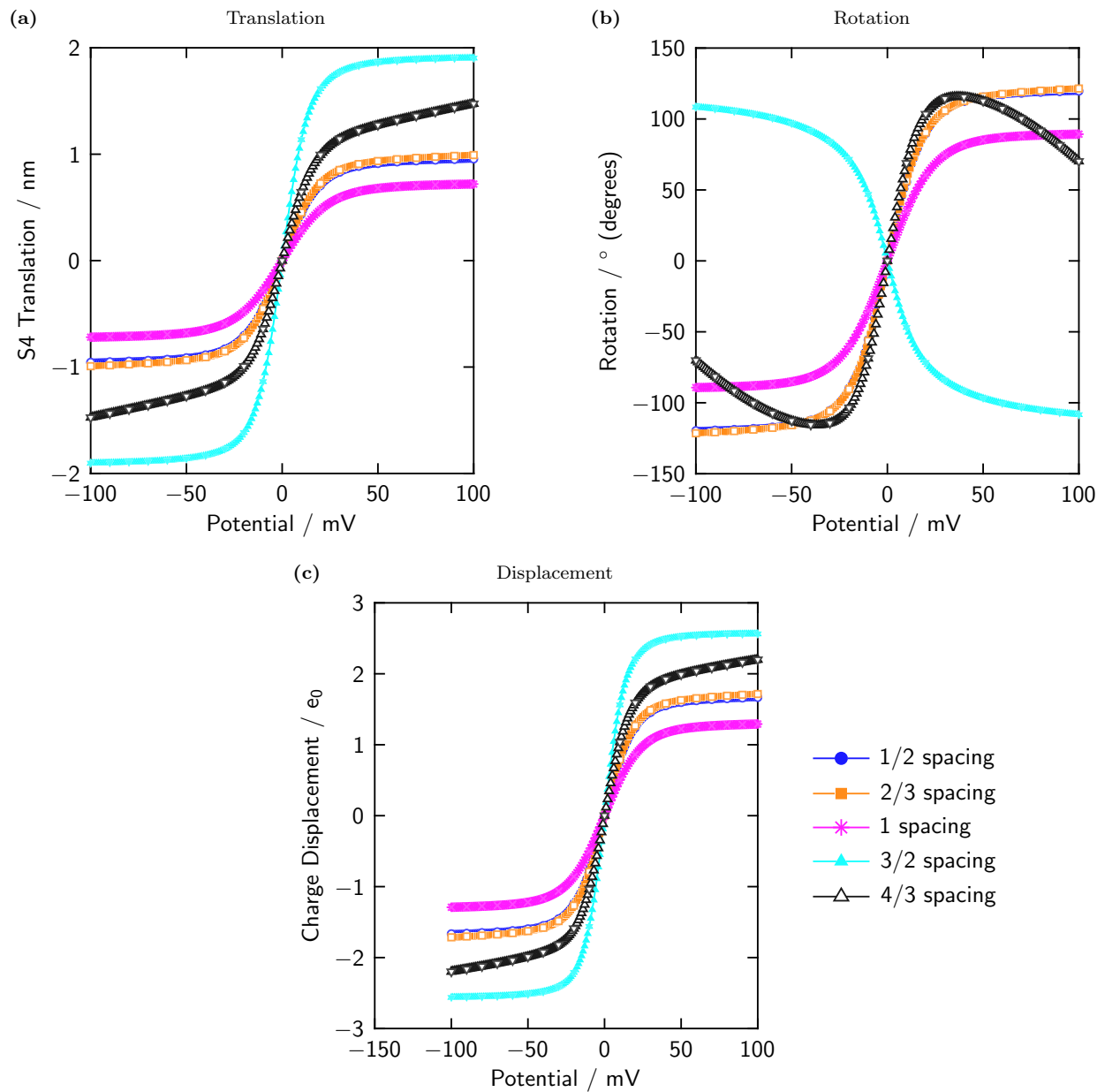


**Figure 3.9: Counter-charge spacing is important for VS response to voltage:** Expectation values of translation (a), rotation (b) and displaced gating charge (c) in response to varied applied voltage. The expectations for these random variables are computed using the electrostatic partition functions for the two degrees of freedom. The same sliding helix models are used as in Figs. 3.7 & 3.8. Counter-charge spacing controls the extent of S4 charge motion, direction of rotation, as well as magnitude of gating charge and shape of the charge/voltage relation. (Note that 1/2 interval in *blue* falls closely on top of 2/3 interval in *orange*).

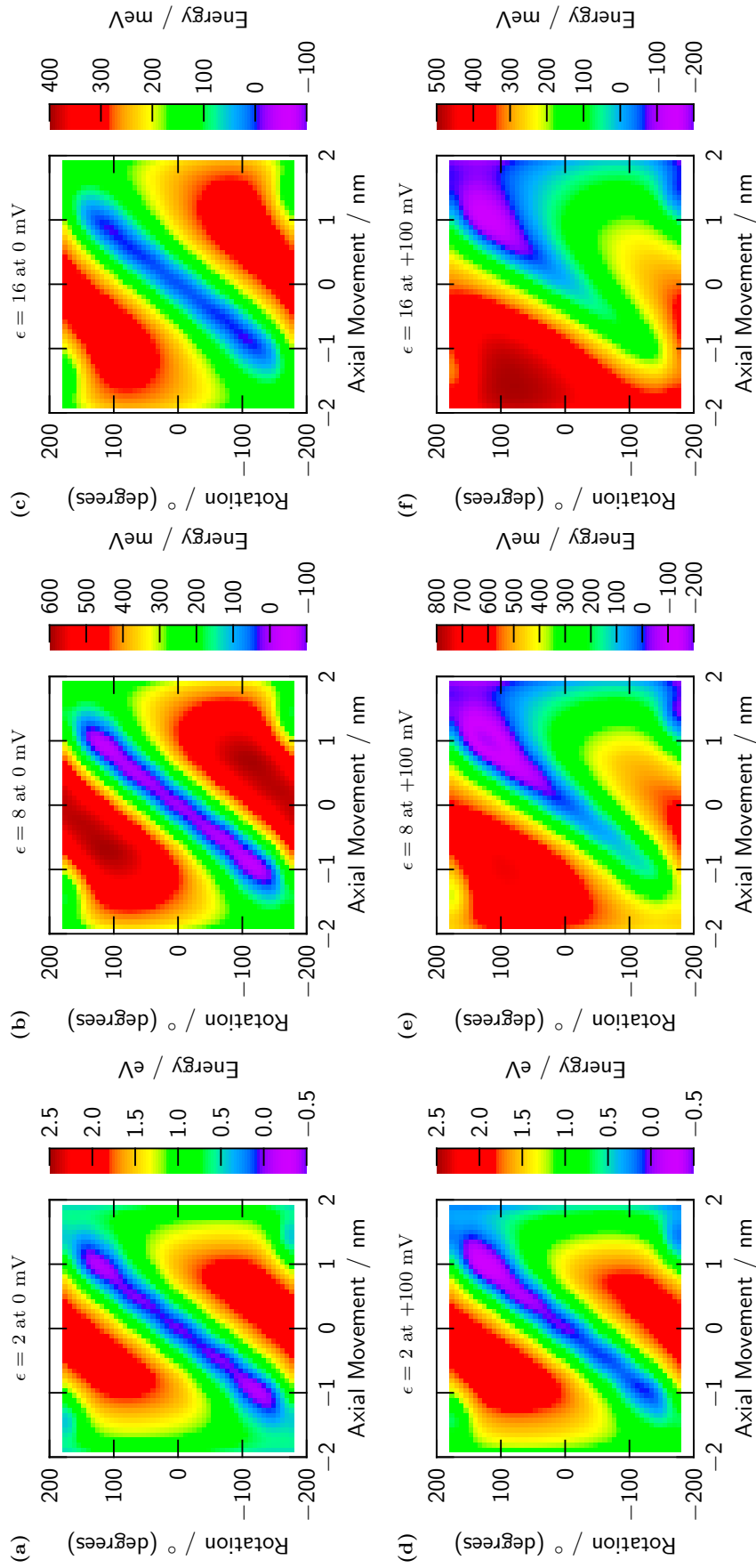


**Figure 3.10: Protein dielectric coefficient constrains the accessible range of motion.** From left to right (panels a-c) the dielectric coefficient  $\epsilon_p$  of S4 and the surrounding protein matrix varies over 2, 8 & 16 for models voltage-clamped at 0 mV with a 2/3 interval (4 is presented in Fig. 3.3). Likewise for +100 mV,  $\epsilon_p$  is varied over 2, 8 & 16 in panels (d-f). The potential energy of each VS configuration relative to translation 0 nm and rotation  $0^\circ$  is represented in false color; note the difference in scales. At  $\epsilon_p = 2$  the range between maxima and minima are  $\approx 3$  eV, while at  $\epsilon_p = 16$  this difference is reduced to  $\approx 0.5$  eV & 0.7 eV.

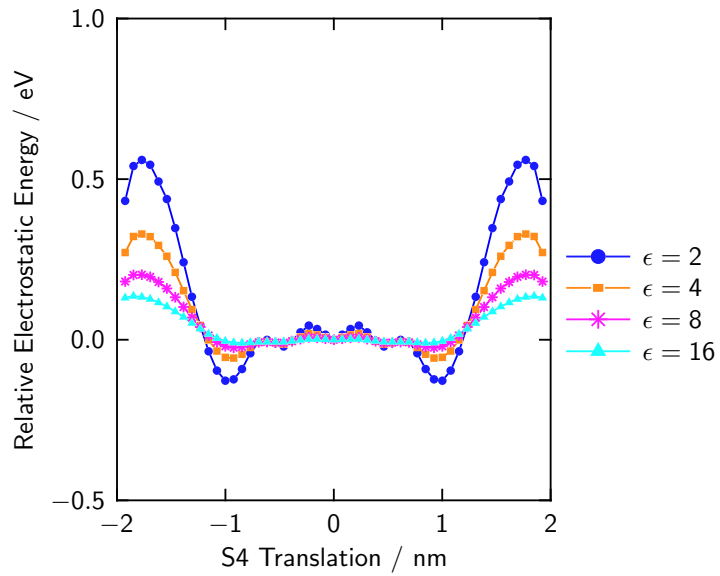


**Figure 3.11: Protein dielectric coefficient constrains the size of energy barriers distinguishing stable configurations.** The electrostatic potential energy at 0 mV and 2/3 interval relative to the 0 translational position is depicted for each translational position from the rotational partition function, as  $\epsilon_p$  is varied over 2 (*blue*), 4 (*orange*), 8 (*magenta*) & 16 (*cyan*). The data for  $\epsilon_p = 4$  is also presented as the blue curve in Fig. 3.3 (d). As  $\epsilon_p$  is increased, the energetic barrier distinguishing  $\pm 1$  nm from each other falls, as well as the barriers constraining S4 to the membrane.

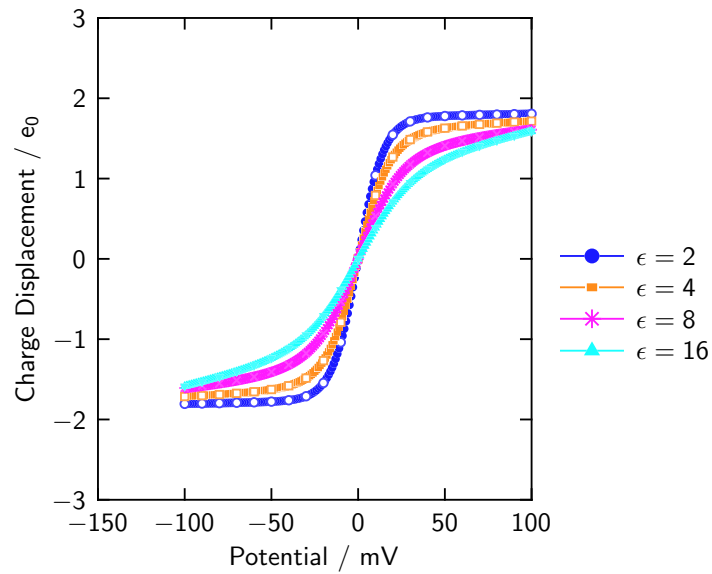


**Figure 3.12: Protein dielectric coefficient constrains the distribution of charge displacement.** As  $\epsilon_p$  is varied over 2 (*blue*), 4 (*orange*), 8 (*magenta*) & 16 (*cyan*), the maximum slope of the charge displacement curve is reduced, while total charge displacement is not. The charge displacement for  $\epsilon_p$  has been previously presented versus experimental results in Fig. 3.5 (c), *blue* curve. All curves were calculated with a 2/3 interval at 0 mV.

and relative positions to each other (Jiang et al., 2003; Long et al., 2005, 2007; Tao et al., 2010), recalling that each of these examples is crystallographic data from a small subset of the full ensemble of conformations of the VS. Motions of the S1–S3 regions of the VS are experimentally undetermined.

The charged residues of the VS have many points of rotation and extend relatively far from the  $\alpha$ -helical backbones to which they are attached (particularly arginine and glutamate residues, Creighton 1984); for example, in Long et al. (2007, Fig. 4), four charge/counter-charge pairs are shown in direct contact despite the S4 appearing to form an angle (and therefore creating a gap) with the S1, S2 and S3 domains. Additionally, there exists ambiguity regarding which charges are permanently situated in the intra- and extracellular solutions and which ones are within the gating pore regions where the ratio of electrical travel to geometrical travel is larger (Nonner et al., 2004, Fig. 2).

However, it is known that three or four counter-charges on the S2 and S3 transmembrane domains are highly conserved depending on which  $K_v$  channels are included (Islas and Sigworth, 1999; Jiang et al., 2003; Tao et al., 2010), and that neutralization of three counter-charges have profound effects on VS behavior (Planells-Cases et al., 1995; Papazian et al., 1995; Seoh et al., 1996). From the results shown in COUNTER-CHARGES ELIMINATE THE INDUCED-CHARGE BARRIER, SUBSEC. 3.3.1, three counter-charges are sufficient to produce VS-like behavior, and fewer charges fail to stabilize the sliding helix in the membrane (data not shown for single and double counter-charge simulations).

The biologically possible configuration space is of high dimensionality, so as a test of the variety of conditions under which the previously elucidated model can function I begin with a reduced model of counter-charge positions and mutations. As described in SLIDING HELIX MODEL, SUBSEC. 2.3.1, charge and counter-charge mutants are modeled both as a simple elimination of the point-charges associated with the residues and by the point-charges' replacement by a dipole to represent the polarizability of glutamine and asparagine residues. The envelope contained by the curves representing these two extreme models of each mutation can be used to investigate the robustness of components of this model (charge elimination is a maximally energetically unfavorable model, whereas the chosen dipole representation is minimally energetically unfavorable).

I have calculated the behavior of models with corresponding charge deletions, testing to what extent the experimental charge/voltage curves are predicted. This requires as-

signing the S2 and S3 negative charges neutralized by Seoh et al. (1996) to counter-charge positions in the sliding helix models. The residues *E283*, *D316*, and *E293* are assigned to the outermost, central, and innermost counter-charge respectively. The counter-charges are spaced at the  $2/3$  interval, and the protein dielectric coefficient is set to 4. In these models when one of the counter-charges is removed, the trough of electrostatic potential energy that confines S4 charge motion (see Fig. 3.6) becomes inverted; therefore the S4 segment is no longer stable in the weak dielectric. On the other hand, mutants with one S2 or S3 negative residue neutralized are functional, indicating that their S4 segments are not dislocated. Therefore, I confine the S4 segment of the models presented in this section within the translational range of  $\pm 1.5$  nm. Charge/voltage curves are computed using the partition function resulting from the electrostatic potential energy of the VS sampled over the rotational and translational degrees of freedom.

Figs. 3.13 through 3.21 summarize the results. Panel (b) of each figure shows the experimental charge/voltage curves for the wildtype channel (*orange squares*) and the mutant (*blue circles*), as reported in Fig. 2 (A–J) of Seoh et al. (1996). Panel (a) of each figure shows the corresponding curves computed for the model. The experimental charge/voltage curves are vertically aligned so that their midpoints correspond to zero displaced charge. There are no horizontal alignments or normalizations except in Fig. 3.13 (Seoh et al., 1996 report in their Fig. 2 E a normalized charge/voltage curve for mutant *R362Q*). All other curves represent charge per VS.

In comparing the computed and experimental results, it is useful to consider differences in the size of wildtype and mutant charges, shifts between wildtype and mutant voltage dependencies, and slope and shape changes between wildtype and mutant. My computations apply to an isolated VS, while the experiments were done on channels; therefore, the 'idle' VS is being compared to the naturally gate-coupled VS. To the extent that the coupling to the gate restricts S4 charge motion and requires work to be done by the VS, it is expected that the gating charge of the model VS is greater than that of the channel VS, and that the charge/voltage curves are shifted with respect to one another. Because VS model and channel charge/voltage curves are expected to be shifted with respect to one another, it is useful to focus on the differences between mutant and wildtype curves. To what extent does the model account for the mutation-versus-wildtype changes?

### 3.4.1 Mutation of a positive charge

Model and experimental results of successively mutating one S4 charge are shown in Figs. 3.13 through 3.16, starting with the outermost arginine residue. In real *Shaker* channels, these mutations produce substantial changes to the charge/voltage relation including reduction of total charge, changes of slope, deformations of the charge/voltage relation and shifts along the voltage axis. The experimental pattern of change varies from mutation to mutation. The predictions from the model reflect the varying experimental patterns very well. Only one qualitative difference is seen: the model does not predict the shift toward negative voltages seen in the *R368N* mutant (Fig. 3.15).

### 3.4.2 Mutation of a negative charge

The results of neutralizing one of a group of putative counter-charges, two glutamate residues of S2 and an aspartate residue of S3, are shown in Figs. 3.17 through 3.19. In the model, these mutations are mimicked by deleting the outermost (*E283*), central (*D316*), and innermost (*E293*) counter-charge. Since these assignments are tentative, testing the model against experiments also tests for the adequacy of the guessed counter-charge to residue assignments.

The comparisons of predicted and experimental mutant effects are, again, surprisingly good. The varying directions and degrees of shift along the voltage axis are predicted quite well. Because the model assigns the first and third in the group of counter-charges to the residues *E283* & *E293* and because of the symmetry in the model's charge configuration, the simulations predict that the Q/V curves for *E283Q* and *E293Q* should reflect such symmetry, but in fact the experimental curves are not symmetric. In particular *E293Q* has a substantially smaller total gating charge than *E283Q*. Thus the VS of the channel has an asymmetry in its structure or operates under asymmetrical constraints that are not included in these VS models. *E283Q* and *D316N* reveal activation curves (not shown) of the ionic current that are strongly shifted to positive voltages. The charge/voltage curves reported by Seoh et al. (1996) do not extend over this voltage range, so they can not reveal the full gating charge.

### 3.4.3 Combined mutations of a positive and a negative charge

The two double mutants investigated by Seoh et al. (1996) are represented in Figs. 3.20 and 3.21. The charge/voltage

curves of the mutants are shifted to negative voltages; the activation curves are also strongly altered (with a left shift in the case of *K374Q + D316N*). The VS of these mutant channels appears to have difficulty in moving into fully-closed positions. The predicted curves reveal limitations of the model. A double mutant lacking two VS charges is expected to be particularly sensitive to the geometry assigned to charges due to the positions and orientations of potential gaps between charges and counter-charges, apart from the already mentioned distinction regarding gating load.

### 3.4.4 Investigation of a mutant lacking functional expression

The double mutations of *K374Q + E293Q* and *K374Q + D316N* by Seoh et al. (1996) were partially motivated by the lack of functional expression by *K374Q* mutants. Since ionic conductance was blocked at all potentials, charge displacement per channel could not be estimated. One could speculate as to the cause of this — whether the VS proper was non-functioning or whether some folding pathology blocked proper expression. Experimentally, there is limited accessibility for non-expressive behavior; however, computational exploration is still possible. In Fig. 3.22, a computational analog of *K374Q* is tested: (1) charge displacement is greatly reduced in panel (a), with some increase extending towards large positive potentials; (2) S4 position is constrained to the intracellular, closed positions in panel (b); and (3) no path for fully moving to the open position is apparent from the potential energy landscapes in panels (c) & (d). The failure of *K374Q* to function biologically is consistent with the predicted electrostatic limitations of *K374Q* as a VS.

### 3.4.5 Summary of mutation simulations

These model studies of charge mutants show that the quality of the model predictions varies in a pattern. S4 charge mutants are described well, S2 and S3 (counter-charge) mutants less well, and double mutants least well. S4 charges likely form a regular array of charges because of the S4's helical structure. Thus the model assumption of uniform spacing of the S4 charges is probably sound. The arrangement of putative counter-charges provided by the S2 and S3 segments has a much larger range of uncertainty, of which I have explored only a small subrange — more exploration is needed.

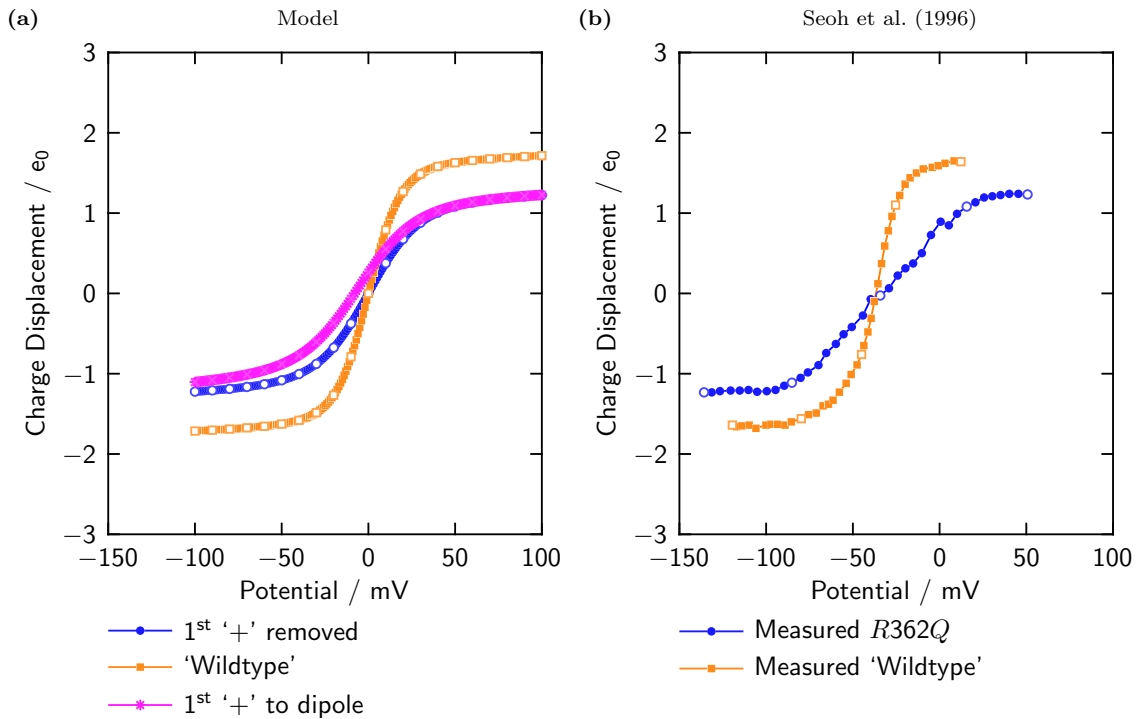


**Figure 3.13: Effective gating charge is reduced by mutating the outermost arginine.** The slope of the QV relation, the effective gating charge, is reduced relative to the wildtype for both the computed and experimental results. Note that Seoh et al. (1996, Fig. 2 E) report for this case normalized charge displacement, so total gating charge is not comparable with wildtype results. Dipole and deletion representations are similar.

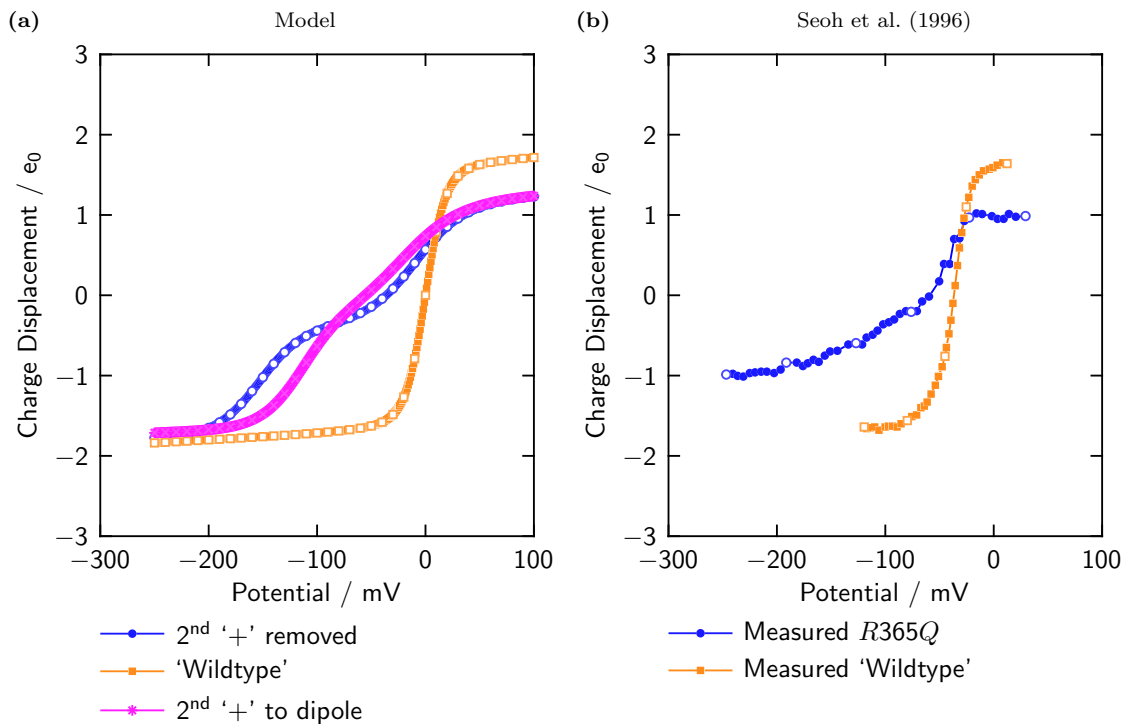


**Figure 3.14: Mutation of the 2<sup>nd</sup> arginine significantly reduces effective charge.** Both computed and experimental results show a left shift. Note the inflection point for the model mutations below -100 mV and the sensitivity to charge representation at extreme negative voltages.



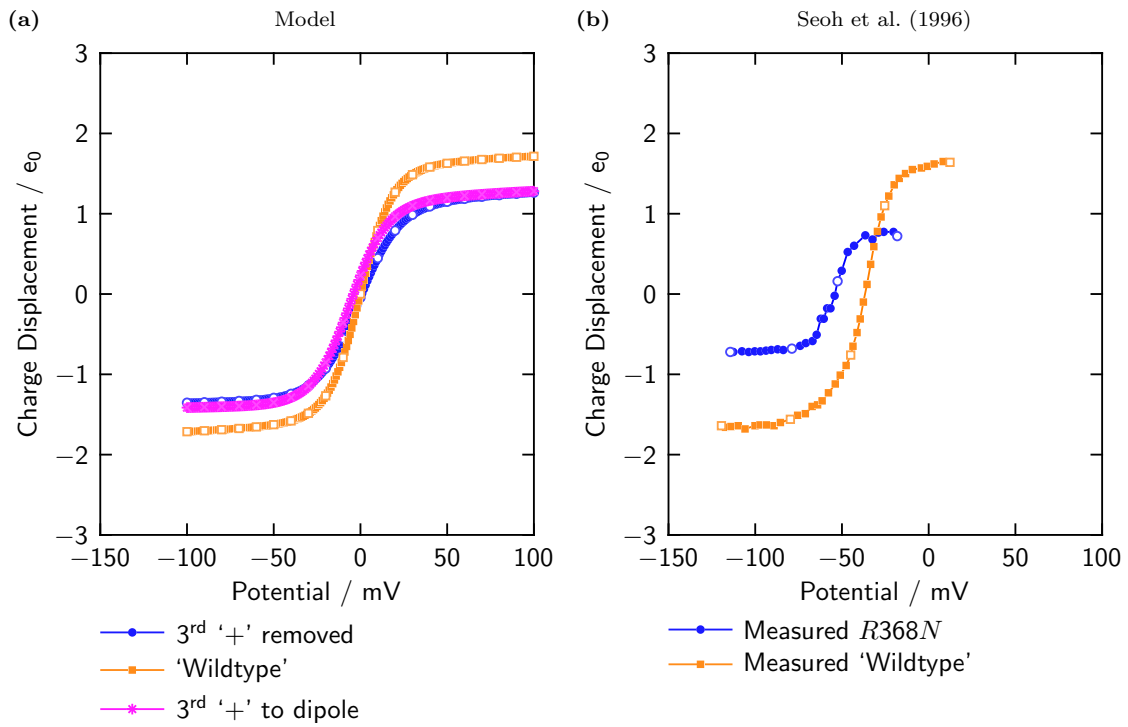


**Figure 3.15: Mutation of the 3<sup>rd</sup> arginine reduces total gating charge.** In this case, experimental results show a left shift that is not apparent in the computational results, combined with an even more significant total reduction in charge. *R368N* also shows a left shift in open probability (data not shown). Dipole and deletion representations are similar.

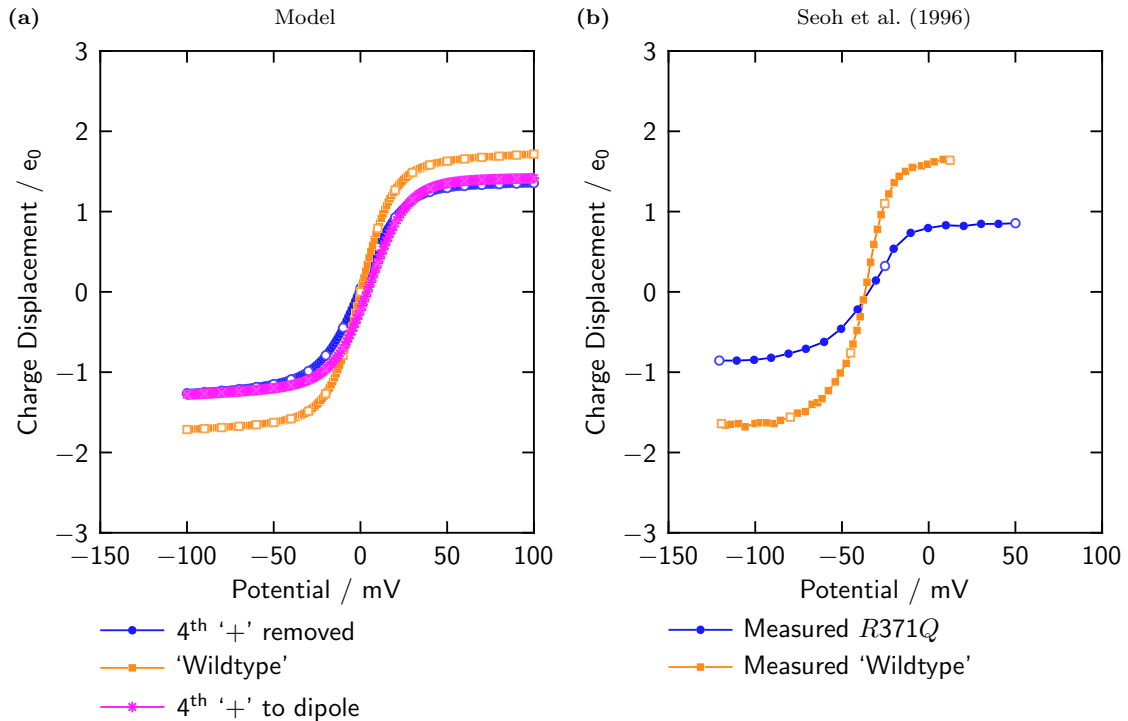


**Figure 3.16: Mutation of the 4<sup>th</sup> arginine reduces total gating current.** Neither results shows a shift in the charge/voltage relationship. Dipole and deletion representations are similar.

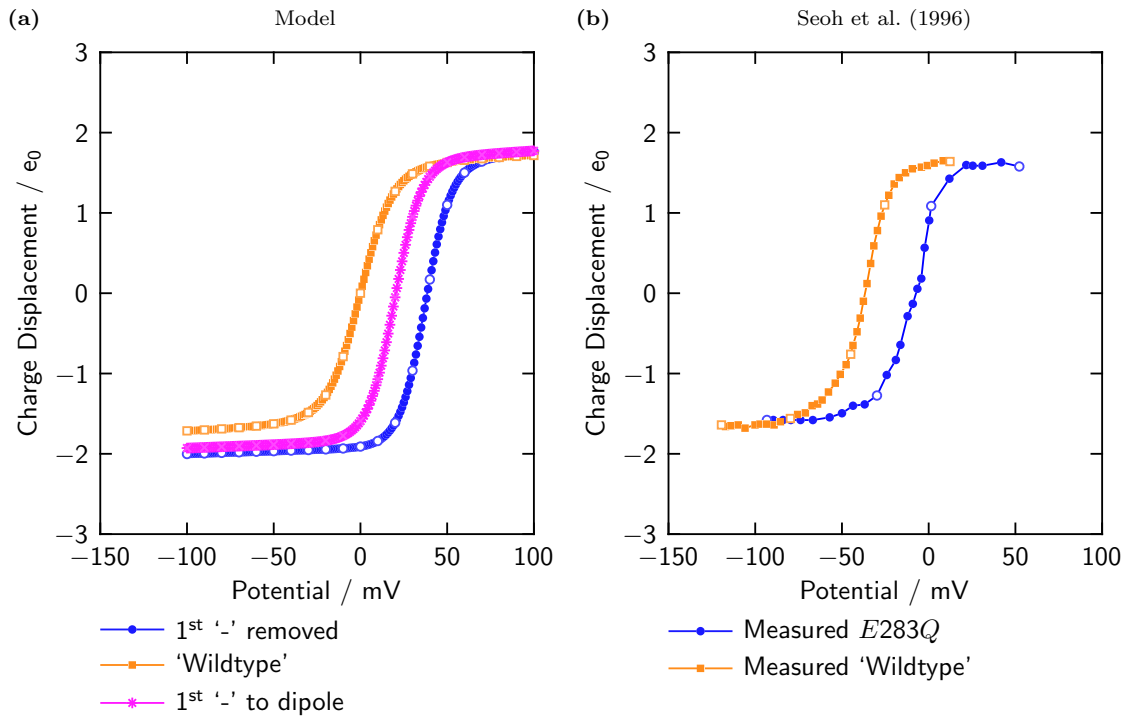


**Figure 3.17: Mutation of the outermost counter-charge produces a right shift with no gating charge reduction.** Experimental results also show a right shift for the open probability (data not shown). Both representations of the mutation are right-shifted and have similar slopes, but the magnitude of the right-shift is distinct.

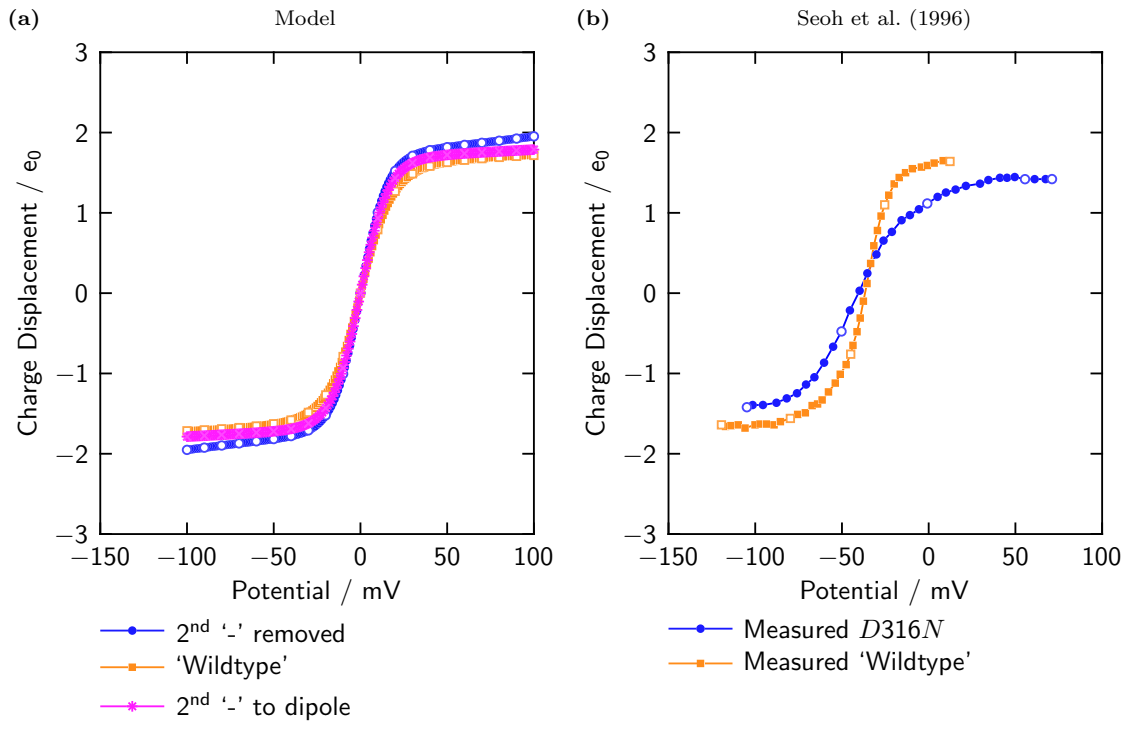


**Figure 3.18: Mutation of the middle counter-charge has a mild effect.** Experimental results show a small reduction in gating charge & slope, while computational results predict a slight increase for both due to the exclusion of S4 from central positions. Dipole and deletion representations are similar.

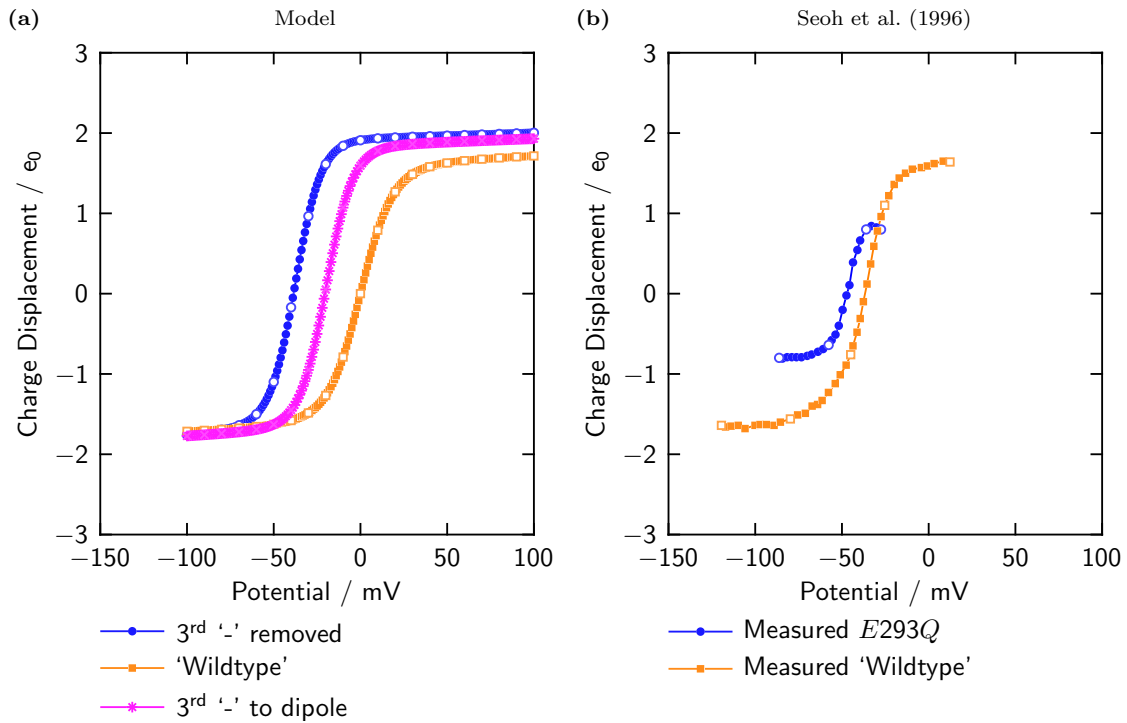


**Figure 3.19: Mutation of the innermost counter charge produces a left shift.** Computational results are symmetrical with 3.17 (a), while experimental results show a large reduction in gating charge which is not apparent in *E283Q*. Experimental results also show a left shift for open probability, as opposed to the right shift for *E283Q* (data not shown). Both representations of the mutation are left-shifted and have similar slopes, but the magnitude of the left-shift is distinct.

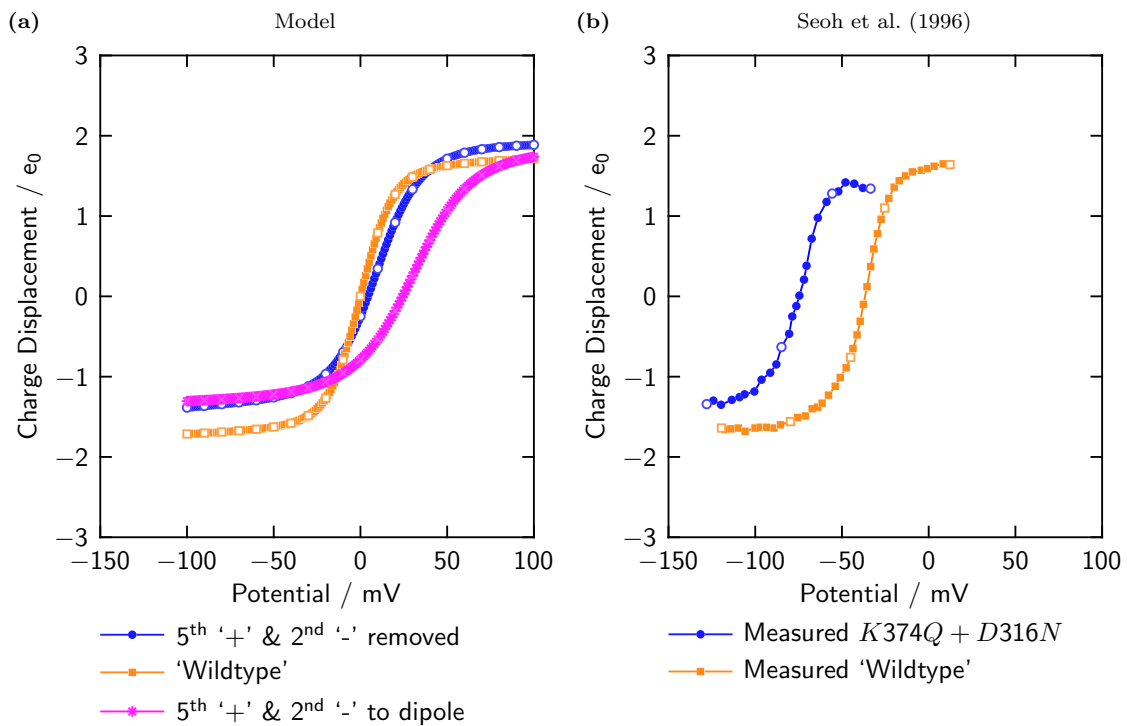


**Figure 3.20: Mutating the outermost lysine & central counter-charge produces a small reduction in total charge displacement.** Experimental results show a left shift that computational results do not reproduce. *K374Q + D316N* also shows a left shift in open probability (data not shown). The dipole representation displays a much larger right-shift and a slightly larger reduction in total charge displacement relative to the deletion representation.

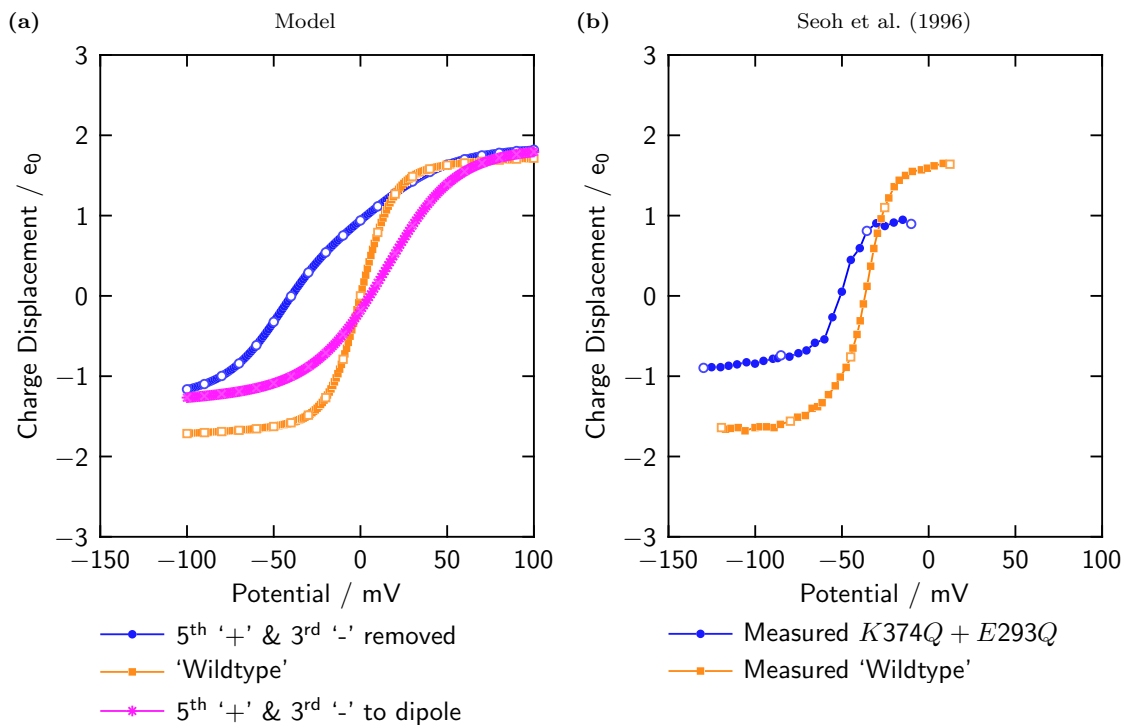


**Figure 3.21: Mutating the outermost lysine & the innermost counter-charge produces a reduction in total gating current.** The computational results for deletion, however, predict a reduction in slope that is replaced by a larger reduction in total gating charge in the experimental results. *K374Q + E293Q* also shows a left shift in open probability (data not shown). The dipole representation fails to predict the left shift of the experimental results reproduced by the deletion representation; however, the dipole representation reproduces the higher slope of the experimental mutant.

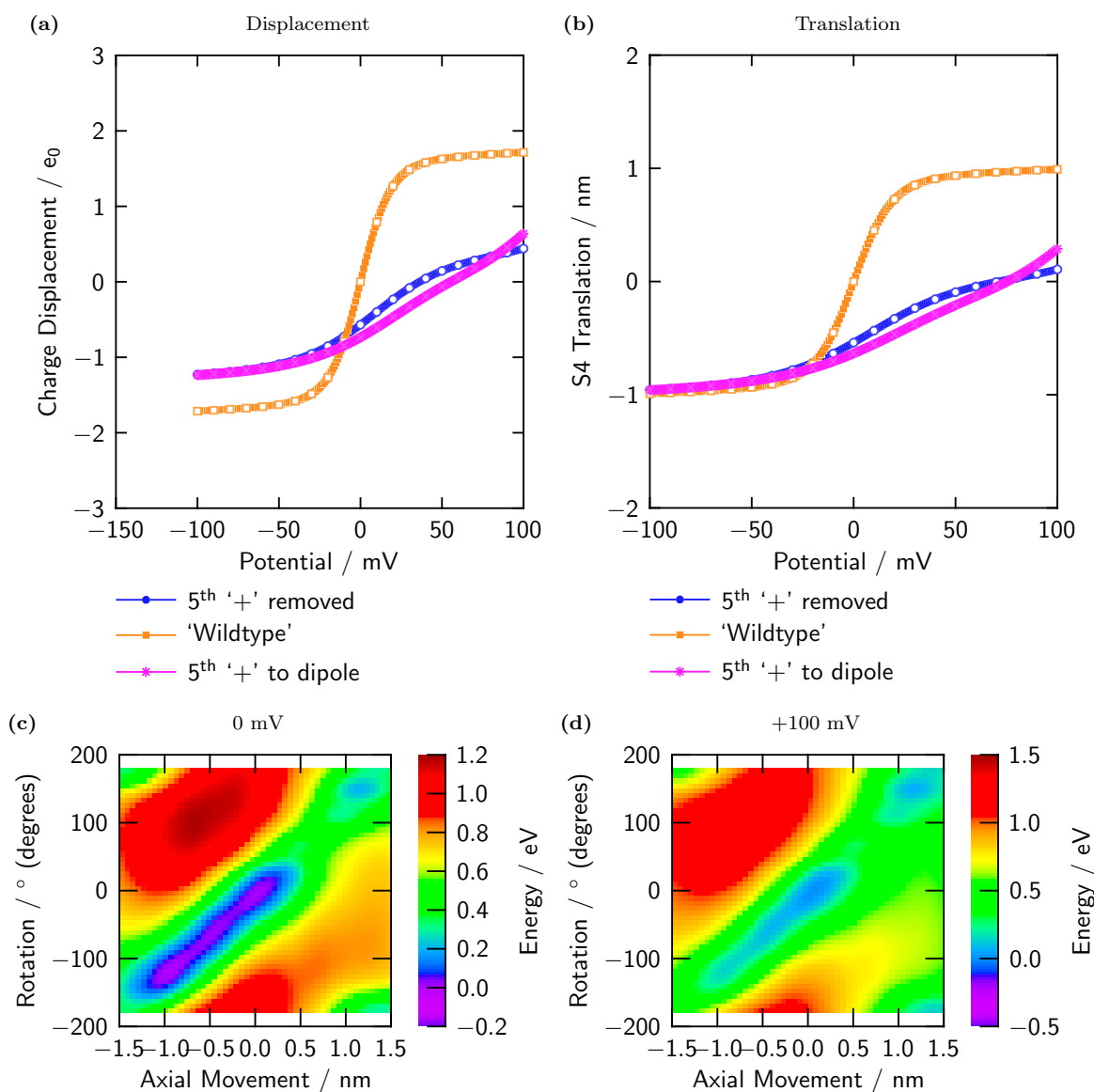


**Figure 3.22: The non-functional *K374Q* mutant is electrostatically incompetent.** Charge displacement in panel (a) is marginal, only reaching  $0 e_0$  at highly positive potentials. The associated translation in panel (b) tracks the gating charge, never moving past the central position until the internal relative electrode potentials approaches +100 mV. In panels (c & d), a large energy barrier at 1 nm is apparent even at +100 mV. Panels (c) and (d) were produced with the deletion representation. Both mutant representations show similar results.

## Chapter 4

# Perspectives

I have developed a computational approach for studying the electrostatics of the voltage sensor (VS) controlling conduction in voltage-dependent ion channels. The VS is described in a microscopic physical model that is reduced in detail to those features whose relevance for VS function is to be investigated. The microscopic model is complemented by a simulation system that establishes voltage-clamp conditions and records gating charge movements in a manner analogous to and comparable with a macroscopic experimental setup. Using efficient computational methods that allow a statistical-mechanical analysis of VS behavior, characteristics that are experimentally accessible (such as the charge/voltage relation) are computed for different models of the VS. My approach thus substantially extends the computational means for studying structure-function relationships of the VS system while making comparisons with experimental results. The presented results provide the following perspectives on the VS.

**How do charged residues ‘contribute’ to gating charge?** Published experiments have sought answers to this question by neutralizing a formally charged residue of the VS and measuring the slope of voltage dependence of activation (Stühmer et al., 1989) or recording ensemble gating charge while counting channels with an independent method such as noise analysis of ionic current (Aggarwal and MacKinnon, 1996; Seoh et al., 1996; Baker et al., 1998; Ledwell and Aldrich, 1999). The results of the latter are expressed as the change (typically reduction) in gating charge per channel. My computational studies show how charge neutralization can modify gating charge in a manner amenable to several modes of analysis: (1) the S4 charge motion carries less charge as a direct consequence of removing one of its charges — the

simplest mode; (2) the range of S4 charge motion becomes electrostatically restricted, leading *all* S4 charges to travel a shorter distance, as they are part of a solid body; and (3) the electrostatic potential energy landscape for S4 travel is altered in such a manner that the probability distribution of positions is altered, with consequences for the shape of Q/V relationships. Modes (2) and (3) may apply regardless of whether the neutralized residue is mobile or fixed in position. Under the latter conditions, the total gating charge can be reduced by an amount greater than the neutralized charge since the motion of all charges is modified by altering one charge.

**Counter-charges to the positively charged S4 residues are essential.** Much discussion of how the S4 helix with its array of positively charged residues might be stabilized in the membrane has focused on the polarizability of the S4 matrix and its environment. The primary requirements for allowing the S4 charges to act as a VS are the proper number and positions of counter-charges. The importance of negatively charged residues for VS function is well established; the respective residues of the S2 and S3 segments are highly conserved (Islas and Sigworth, 1999; Tao et al., 2010), and neutralization mutants show strong alterations of function (Seoh et al., 1996).

Computationally, I find that a viable VS model includes counter-charges. Removing counter-charges from the model creates a landscape of electrostatic potential energy that tends to exclude the S4 charged region from the membrane region — a large barrier develops from charge induced on the bath interface by buried, unbalanced S4 charges. This happens in the presence of deep gating pores that reduce the number of buried S4 charges to no more than three. My computations show that much of the observed consequences of

neutralization mutants on S2, S3, and S4 can be understood on electrostatic grounds as resulting from the charge/counter-charge interactions among the buried residues and the charges that they induce on dielectric boundaries. The computational results for a reduced electrostatic model suggest that the charge/counter-charge interactions in the VS warrant detailed investigation.

**Electrostatics dominate.** The fact that a model solely including electrostatic interactions reproduces many experimental phenomena reveals the primary importance of electrostatics in the VS system. Reduced models focused on elec-

trostatic interactions can thus provide essential insights into experimental behavior.

My simulations assemble a handful of positive and negative charges, enclose them in a reflective dielectric boundary, reshuffle their configurations with an external field and provide an experimental window for viewing. The result is a kaleidoscope. A “simple” electrostatic system produces complex phenomena which appear to be more easily understood by constructing the mechanism of the kaleidoscope than by inferring the mechanism via induction from the phenomena viewed through it.

# Bibliography

- Sanjay Kumar Aggarwal and Roderick MacKinnon. Contribution of the S4 segment to gating charge in the *Shaker* K<sup>+</sup> channel. *Neuron*, 16(6), 1 June 1996. URL <http://www.sciencedirect.com/science/article/B6WSS-41BMYRR-G/2/16634e29ee68d83e66d15ab25313a7f3>.
- C.M. Armstrong and F. Bezanilla. Currents related to movement of the gating particles of the sodium channels. *Nature*, 242(5398):459–461, 13 April 1973. doi: 10.1038/242459a0. URL <http://www.nature.com/nature/journal/v242/n5398/abs/242459a0.html>.
- O.S. Baker, H.P. Larsson, L.M. Mannuzzu, and E.Y. Isacoff. Three transmembrane conformations and sequence-dependent displacement of the S4 domain in *Shaker* K<sup>+</sup> channel gating. *Neuron*, 20(6):1283–1294, 1998.
- J. Barthel, R. Buchner, and M. Münsterer. *Electrolyte Data Collection Pt. 2: Dielectric Properties of Water and Aqueous Electrolyte Solutions*, volume 12 of *Chemistry Data Series*. DECHEMA, Deutsche Gesellschaft für Chemisches Apparatewesen, Chemische Technik und Biotechnologie e.V., Frankfurt am Main, FRG, 1995.
- Audrey A. Bliznyuk and Alistair P. Rendell. Electronic effects in biomolecular simulations: Investigation of the KcsA potassium ion channel. *J. Phys. Chem. B*, 108:13866–13873, 2004. doi: 10.1021/jp0487298. URL <http://pubs.acs.org/cgi-bin/abstract.cgi/jpcb/fk/2004/108/i36/abs/jp0487298.html>.
- Dezső Boda, Dirk Gillespie, Wolfgang Nonner, Douglas Henderson, and Bob Eisenberg. Computing induced charges in inhomogeneous dielectric media: Application in a Monte Carlo simulation of complex ionic systems. *Phys. Rev. E*, 69(4):046702, 21 May 2004. doi: 10.1103/PhysRevE.63.046702. URL <http://link.aps.org/abstract/PRE/v69/e046702>.
- H.J. Bowdler, R.S. Martin, G. Peters, and J.H. Wilkinson. Solution of real and complex systems of linear equations. In F.L. Bauer, A.S. Householder, F.W.J. Olver, H. Rutishauser, K. Samelson, and E. Stiefel, editors, *Linear Algebra*, volume II of *Handbook for Automatic Computation*, contribution I/7, pages 93–110. Springer-Verlag, 1971.
- W. A. Catterall. Structure and function of voltage-sensitive ion channels. *Science*, 242(4875):50–61, Oct 1988. doi: 10.1126/science.2459775. URL <http://www.sciencemag.org/cgi/content/abstract/sci;242/4875/50>.
- W.A. Catterall. Molecular properties of voltage-sensitive sodium channels. *Annu. Rev. Biochem.*, 55:953–858, 1986.
- Sudha Chakrapani, Luis G Cuello, D. Marien Cortes, and Eduardo Perozo. Structural dynamics of an isolated voltage-sensor domain in a lipid bilayer. *Structure*, 16(3):398–409, Mar 2008. doi: 10.1016/j.str.2007.12.015. URL <http://dx.doi.org/10.1016/j.str.2007.12.015>.
- W. K. Chandler and H. Meves. Voltage clamp experiments on internally perfused giant axons. *J Physiol*, 180(4):788–820, Oct 1965. URL <http://jp.physoc.org/content/180/4/788.full.pdf+html>.
- David Leonard Chapman. A contribution to the theory of electrocapillarity. *Philosophical Magazine Series 6*, 25(148):475–481, 1913. ISSN 1941-5982. URL <http://www.informaworld.com/10.1080/14786440408634187>.
- Thomas E. Creighton. Chemical nature of polypeptides. In *Proteins: Structures and Molecular Properties*, chapter 1, pages 2–60. W.H. Freeman and Company, 1984.
- P. Debye and E. Hückel. The theory of electrolytes. I. Lowering of freezing point and related phenomena. *Physikalische Zeitschrift*, 24:185–206, 1923.



- D.A. Doyle, J. Morais Cabral, R.A. Pfuetzner, A. Kuo, J.M. Gulbis, S.L. Cohen, B.T. Chait, and R. MacKinnon. The structure of the potassium channel: Molecular basis of  $K^+$  conduction and selectivity. *Science*, 280:69–77, 1998.
- R. P. Feynman, R. B. Leighton, and M. Sands. Electromagnetism. In *The Feynman Lectures on Physics: Mainly Electromagnetism and Matter*, volume II, chapter 1. Addison-Wesley Publishing Co., New York, USA, 1963.
- Richard P. Feynman. Introduction to statistical mechanics. In *Statistical Mechanics: A Set of Lectures*, chapter 1, pages 1–38. Addison-Wesley Longman, Inc., 1988.
- G. Gouy. Sur la constitution de la charge électrique à la surface d’un électrolyte. *Compt. Rend.*, 149:654–657, 1909.
- Michael Grabe, Harold Lecar, Yuh Nung Jan, and Lily Yeh Jan. A quantitative assessment of models for voltage-dependent gating of ion channels. *PNAS*, 101(51):17640–17645, 2004. URL <http://www.pnas.org/cgi/content/abstract/101/51/17640>.
- D.J Griffiths. *Introduction to Electrodynamics*. Prentice Hall, Upper Saddle River, New Jersey, USA, 3rd edition, 1999a.
- D.J Griffiths. Electrostatics. In *Introduction to Electrodynamics* Griffiths (1999a), chapter 2, pages 58–109.
- D.J Griffiths. Electric fields in matter. In *Introduction to Electrodynamics* Griffiths (1999a), chapter 2, pages 160–193.
- Zhong He. Review of the Shockley-Ramo theorem and its application in semiconductor gamma-ray detectors. *Nuclear Instruments and Methods in Physics Research Section A: Accelerators, Spectrometers, Detectors and Associated Equipment*, 463(1–2):250–267, 2001. ISSN 0168-9002. doi: 10.1016/S0168-9002(01)00223-6. URL <http://www.sciencedirect.com/science/article/B6TJM-4313P16-V/2/8667fbb09402eb8fc6d245f1d04b1e7c>.
- Bertil Hille. Gating mechanisms: Kinetic thinking. In *Ion Channels of Excitable Membranes*, chapter 18. Sinauer Associates, Inc., Sunderland, Mass. USA, 3rd edition, 2001.
- A.L. Hodgkin and A.F. Huxley. Movement of sodium and potassium ions during nervous activity. In *Cold Spring Harb. Symp. Quant. Biol.* Ian Cooke and Mack Lipkin (1972), pages 43–52.
- A.L. Hodgkin and A.F. Huxley. A quantitative description of membrane current and its application to conduction and excitation in nerve. In *J. Physiol.* Ian Cooke and Mack Lipkin (1972), pages 500–544.
- T. Hoshi, W. N. Zagotta, and R. W. Aldrich. Biophysical and molecular mechanisms of shaker potassium channel inactivation. *Science*, 250(4980):533–538, Oct 1990.
- William Humphrey, Andrew Dalke, and Klaus Schulten. VMD: Visual molecular dynamics. *J. of Mol. Graphics*, 14(1):33–38, February 1996. URL <http://www.sciencedirect.com/science/article/B6VNC-3VJRDJX-5/2/247595492d1cae80b34bed4d649bf0b2>.
- Ian Cooke and Jr. Mack Lipkin, editors. *Cellular Neurophysiology: A Source Book*. Holt, Rinehart and Winston, Inc., 1972.
- Leon D. Islas and Fred J. Sigworth. Voltage sensitivity and gating charge in *Shaker* and *Shab* family potassium channels. *J. Gen. Physiol.*, 114(5):723–742, 1999. doi: 10.1085/jgp.114.5.723. URL <http://jgp.rupress.org/cgi/content/abstract/114/5/723>.
- Leon D. Islas and Fred J. Sigworth. Electrostatics and the gating pore of *Shaker* potassium channels. *J. Gen. Physiol.*, 117(1):69–90, 2001. URL <http://www.jgp.org/cgi/content/abstract/117/1/69>.
- John David Jackson. *Classical Electrodynamics*. John Wiley & Sons, Inc., New York, USA, 3rd edition, 1999a.
- John David Jackson. Introduction and survey. In *Classical Electrodynamics* Jackson (1999a), chapter I, pages 1–23.
- John David Jackson. Introduction to electrostatics. In *Classical Electrodynamics* Jackson (1999a), chapter 1, pages 24–56.
- John David Jackson. Multipoles, electrostatics of macroscopic media, dielectrics. In *Classical Electrodynamics* Jackson (1999a), chapter 4, pages 145–173.
- Y. N. Jan, L. Y. Jan, and M. J. Dennis. Two mutations of synaptic transmission in *Drosophila*. *Proc R Soc Lond B Biol Sci*, 198(1130):87–108, Jul 1977.

- Youxing Jiang, Alice Lee, Jiayun Chen, Vanessa Ruta, Martine Cadene, Brian T. Chait, and Roderick MacKinnon. X-ray structure of a voltage-dependent  $K^+$  channel. *Nature*, 423(6935):33–41, 1 May 2003.
- Fatemeh Khalili-Araghi, Vishwanath Jogini, Vladimir Yarov-Yarovoy, Emad Tajkhorshid, Benoît Roux, and Klaus Schulten. Calculation of the gating charge for the Kv1.2 voltage-activated potassium channel. *Biophys J*, 98(10):2189–2198, May 2010. doi: 10.1016/j.bpj.2010.02.056. URL <http://dx.doi.org/10.1016/j.bpj.2010.02.056>.
- Attila Kumanovics, Gal Levin, and Paul Blount. Family ties of gated pores: evolution of the sensor module. *FASEB J*, 16(12):1623–1629, 2002. doi: 10.1096/fj.02-0238hyp. URL <http://www.fasebj.org/cgi/content/abstract/16/12/1623>.
- Jennifer L. Ledwell and Richard W. Aldrich. Mutations in the S4 region isolate the final voltage-dependent cooperative step in potassium channel activation. *J. Gen. Physiol.*, 113(3):389–414, 1999. URL <http://www.jgp.org/cgi/content/abstract/113/3/389>.
- Hwa C. Lee, Julia M. Wang, and Kenton J. Swartz. Interaction between extracellular hanatoxin and the resting conformation of the voltage-sensor paddle in  $K_v$  channels. *Neuron*, 40(3), 30 October 2003. URL <http://www.sciencedirect.com/science/article/B6WSS-4B3MJP2-D/2/c44f01944b603e9b9d2bc1f58d26e1b1>.
- Seok-Yong Lee, Alice Lee, Jiayun Chen, and Roderick MacKinnon. Structure of the KvAP voltage-dependent  $K^+$  channel and its dependence on the lipid membrane. *PNAS*, page 0507651102, 2005. URL <http://www.pnas.org/cgi/content/abstract/0507651102v1>.
- Stephen B. Long, Ernest B. Campbell, and Roderick MacKinnon. Crystal structure of a mammalian voltage-dependent *Shaker* family  $K^+$  channel. *Science*, 309(5736):897–903, 2005. URL <http://www.sciencemag.org/cgi/content/abstract/309/5736/897>.
- Stephen B. Long, Xiao Tao, Ernest B. Campbell, and Roderick MacKinnon. Atomic structure of a voltage-dependent  $K^+$  channel in a lipid membrane-like environment. *Nature*, 450(7168):376–382, 2007. URL <http://dx.doi.org/10.1038/nature06265>.
- P. Lozano-Casal, D. R. Allan, and S. Parsons. High-pressure structural study of L-alpha-glutamine and the use of Hirshfeld surfaces and graph-set notation to investigate the hydrogen bonding present in the structure up to 4.9 GPa. *Acta Crystallogr B*, 64(Pt 4):466–475, Aug 2008. doi: 801793X. URL <http://dx.doi.org/801793X>.
- Kamran C. Melikov, Vadim A. Frolov, Arseniy Shcherbakov, Andrey V. Samsonov, Yury A. Chizmadzhev, and Leonid V. Chernomordik. Voltage-induced nonconductive pre-pores and metastable single pores in unmodified planar lipid bilayer. *Biophys. J.*, 80(4):1829–1836, 2001. URL <http://www.biophysj.org/cgi/content/abstract/80/4/1829>.
- B. Neumcke, W. Nonner, and R. Stämpfli. Gating currents in excitable membranes. *International Review of Biochemistry, Biochemistry of Cell Walls and Membranes II*, 19:129–155, 1978.
- Manami Nishizawa and Kazuhisa Nishizawa. Molecular dynamics simulation of  $K_v$  channel voltage sensor helix in a lipid membrane with applied electric field. *Biophys J*, 95(4):1729–1744, Aug 2008. doi: 10.1529/biophysj.130658. URL <http://dx.doi.org/10.1529/biophysj.130658>.
- M. Noda, T. Ikeda, T. Kayano, H. Suzuki, H. Takeshima, M. Kurasaki, H. Takahashi, and S. Numa. Existence of distinct sodium channel messenger RNAs in rat brain. *Nature*, 320(6058):188–192, 13 March 1986. doi: doi:10.1038/320188a0. URL <http://www.nature.com/nature/journal/v320/n6058/abs/320188a0.html>.
- Wolfgang Nonner, Alexander Peyser, Dirk Gillespie, and Bob Eisenberg. Relating microscopic charge movement to macroscopic currents: The Ramo-Shockley theorem applied to ion channels. *Biophys. J.*, 87(6):3716–3722, December 2004. doi: 10.1529/biophysj.104.047548. URL <http://www.biophysj.org/cgi/content/abstract/87/6/3716>.
- D. M. Papazian, X. M. Shao, S. A. Seoh, A. F. Mock, Y. Huang, and D. H. Wainstock. Electrostatic interactions of S4 voltage sensor in *Shaker*  $K^+$  channel. *Neuron*, 14(6):1293–1301, Jun 1995.
- A. Parsegian. Energy of an ion crossing a low dielectric membrane: Solutions to four relevant electrostatic problems. *Nature*, 221(183):844–846, 1 March 1969. doi: 10.

- 1038/221844a0. URL <http://www.nature.com/nature/journal/v221/n5183/abs/221844a0.html>.
- Linus Pauling. Types of resonance in molecules. In *The Nature of the Chemical Bond*, chapter 8, pages 265–309. Cornell University Press, 3rd edition, 1960.
- E. Perozo, R. MacKinnon, F. Bezanilla, and E. Stefani. Gating currents from a nonconducting mutant reveal open-closed conformations in *Shaker* K<sup>+</sup> channels. *Neuron*, 11(2):353–358, 1993. URL <http://www.neuron.org/content/article/abstract?uid=PII0896627393901903>.
- R. Planells-Cases, A. V. Ferrer-Montiel, C. D. Patten, and M. Montal. Mutation of conserved negatively charged residues in the S2 and S3 transmembrane segments of a mammalian K<sup>+</sup> channel selectively modulates channel gating. *Proc Natl Acad Sci U S A*, 92(20):9422–9426, Sep 1995.
- Simon Ramo. Currents induced by electron motion. *Proc. IRE.*, 27:584–585, 1939. URL <http://www.jneurosci.org/cgi/reprint/27/2/270.pdf>.
- I. Scott Ramsey, Magdalene M. Moran, Jayhong A. Chong, and David E. Clapham. A voltage-gated proton-selective channel lacking the pore domain. *Nature*, 440(7088):1213–1216, April 2006. ISSN 0028-0836. URL <http://dx.doi.org/10.1038/nature04700>.
- Nathan E. Schoppa, Ken McCormack, Mark A. Tanouye, and Fred J. Sigworth. The size of gating charge in wild-type and mutant *Shaker* potassium channels. *Science*, 255(5052):1712–1715, 27 March 1992. URL <http://www.jstor.org/stable/2876643>.
- Sang-Ah Seoh, Daniel Sigg, Diane M. Papazian, and Francisco Bezanilla. Voltage-sensing residues in the S2 and S4 segments of the *Shaker* K<sup>+</sup> channel. *Neuron*, 16(6), 1 June 1996. URL <http://www.sciencedirect.com/science/article/B6WSS-41BMYRR-F/2/d7f99b5e923706ce6f3817570fbc139>.
- W. Shockley. Currents to conductors induced by a moving point charge. *J. Appl. Phys.*, 9(10):635–636, 1938.
- Daniel Sigg, Enrico Stefani, and Francisco Bezanilla. Gating current noise produced by elementary transitions in *Shaker* potassium channels. *Science*, 264(5158):578–582, 22 April 1994. URL <http://www.jstor.org/stable/2883712>.
- Daniel Sigg, Francisco Bezanilla, and Enrico Stefani. Fast gating in the *Shaker* K<sup>+</sup> channel and the energy landscape of activation. *PNAS*, 100(13):7611–7615, 24 June 2003. URL <http://www.pnas.org/cgi/content/abstract/100/13/7611>.
- W. Stühmer, F. Conti, H. Suzuki, X.D. Wang, M. Noda, N. Yahagi, H. Kubo, and S. Numa. Structural parts involved in activation and inactivation of the sodium channel. *Nature*, 339(6226):597–603, 22 June 1989. doi: 10.1038/339597a0. URL <http://www.nature.com/doifinder/10.1038/339597a0>.
- Xiao Tao, Alice Lee, Walrati Limapichat, Dennis A. Dougherty, and Roderick MacKinnon. A gating charge transfer center in voltage sensors. *Science*, 328(5974):67–73, 2010. doi: 10.1126/science.1185954. URL <http://www.sciencemag.org/cgi/content/abstract/328/5974/67>.
- Gregory C. Troiano, Leslie Tung, Vinod Sharma, and Kathleen J. Stebe. The reduction in electroporation voltages by the addition of a surfactant to planar lipid bilayers. *Biophys. J.*, 75(2):880–888, 1998. URL <http://www.biophysj.org/cgi/content/abstract/75/2/880>.
- R. Clint Whaley and Jack Dongarra. Automatically Tuned Linear Algebra Software. Technical Report UT-CS-97-366, University of Tennessee, December 1997. URL <http://www.netlib.org/lapack/lawns/lawn131.ps>.
- N. Yang, A.L. Jr. George, and R. Horn. Molecular basis of charge movement in voltage-gated sodium channels. *Neuron*, 16(1):113–122, 1996.